



저작자표시-비영리-변경금지 2.0 대한민국

이용자는 아래의 조건을 따르는 경우에 한하여 자유롭게

- 이 저작물을 복제, 배포, 전송, 전시, 공연 및 방송할 수 있습니다.

다음과 같은 조건을 따라야 합니다:



저작자표시. 귀하는 원저작자를 표시하여야 합니다.



비영리. 귀하는 이 저작물을 영리 목적으로 이용할 수 없습니다.



변경금지. 귀하는 이 저작물을 개작, 변형 또는 가공할 수 없습니다.

- 귀하는, 이 저작물의 재이용이나 배포의 경우, 이 저작물에 적용된 이용허락조건을 명확하게 나타내어야 합니다.
- 저작권자로부터 별도의 허가를 받으면 이러한 조건들은 적용되지 않습니다.

저작권법에 따른 이용자의 권리는 위의 내용에 의하여 영향을 받지 않습니다.

이것은 [이용허락규약\(Legal Code\)](#)을 이해하기 쉽게 요약한 것입니다.

[Disclaimer](#)

공학박사 학위논문

**Removal of Released Pollutant
with Element Modified
Eco-friendly Biomineral**

조성제어된 생무기물을 이용한
방출된 오염물질 제거

2022년 8월

서울대학교 대학원

재료공학부

홍정석

Removal of Released Pollutant with Element Modified Eco-friendly Biomineral

지도 교수 남 기 태

이 논문을 공학박사 학위논문으로 제출함

2022년 6월

서울대학교 대학원

재료공학부

홍 정 석

홍정석의 공학박사 학위논문을 인준함

2022년 6월

위 원 장 장 호 원 (인)

부위원장 남 기 태 (인)

위 원 김 진 영 (인)

위 원 정 현 석 (인)

위 원 진 경 석 (인)

Abstract

Removal of Released Pollutant with Element Modified Eco-friendly Biomineral

Jung Sug Hong

Department of Materials Science and Engineering

The Graduate School

Seoul National University

Keyword: Carbonate hydroxyapatite, Whitlockite, wet precipitation, CO₂ absorption, Pb absorption, element modification

Student Number: 2014-22535

The biggest issue in 21st century is environmental pollution and enormous efforts were done to deal with problem. Air pollution derived by overuse of fossil fuel caused global warming. CO₂ concentration in the air maintained below 300 ppm over the past 400,000 years, but atmospheric CO₂ level exceeded 400 ppm and continues to increase. Alternative renewable energies are under development to substitute fossil fuel and reduce CO₂ emission, but CO₂ in the air should be retrieved to return to the past. Furthermore, water pollution of heavy metal is also severe environmental pollution which is known for centuries but not yet solved. Lead(Pb), well know heavy metal, causes severe damage to human body and eco-system. Nevertheless, Demand of lead increases as demand of electric lead battery and usage of coal containing lead increases.

Managing entire process from manipulation to post treatment of purification is essential to eliminate the environmental pollutants. Especially, pollution generated

during synthesis of absorbent and post treatment of absorbent are neglected. Large energy cost and pollutant emission is done during synthesis and regeneration process in recent studies. In case of CO₂ absorption, low CO₂ concentration of ambient air is the main obstacle to overcome. Absorbents needs high temperature for operation and regeneration due to its low concentration. CaO needs high temperature over 700 °C in operation and regeneration, wet precipitation method using NaOH needs 900 °C temperature for CaCO₃ calcination.[1,2]

Overall pollution control throughout the entire purification process was done in this research. First, eco-friendly and eco-friendly synthesizable biomineral, Hydroxyapatite, was chosen to solve the problem. Then elemental composition was modified to enhance the activity of absorbent. CO₂ substituted PO₄³⁻ of Hydroxyapatite in the form of CO₃²⁻ and metal cation was modified with Mg to enhance absorption performance of Pb.

In Chapter 1, CO₂ absorption with biomineral in ambient air was studied. To absorb CO₂ in ambient air, wet precipitation method was used as Ca is one of the alkaline earth metals which can absorb CO₂ dissolved in the solution. H₂O₂ was introduced to enhance CO₂ absorption as superoxide generates under reaction with H₂O₂ and alkaline earth metal hydroxide. Captured CO₂ was then used to synthesize Carbonate Hydroxyapatite for upcycling. Avoiding high temperature calcination of CaCO₃ and utilization into biomineral solved additional pollution during air purification.

In Chapter 2, HAP was modified into Whitlockite which is biomineral that contains Mg at metal site with Ca. Dissolution and precipitation mechanism is much faster than Ionic exchange when metal cation substitutes into HAP. Instead of ionic exchange dominant HAP, Whitlockite was used to remove Pb²⁺ cation of the

solution, which dissolution and precipitation is dominant in metal cation substitution. $\text{Mg}(\text{OH})_2$ and additional heat was introduced in synthesis procedure to modify metal element of HAP. WH successfully removed Pb^{2+} ion from the solution, forming Hydroxypyromorphite with high purity and crystallinity. Absorbed Pb was then utilized into PbI_2 , a precursor for perovskite solar cell, with simple treatment. Absorbing Pb via simple dispersion in solution and utilizing Pb as a chemical precursor achieved goal to avoid unintended pollution during purification process.

In this research, released pollutant to air and water was removed with element modified biomineral. Atmospheric CO_2 is captured during synthesis of Carbonate Hydroxyapatite(CHA) and Pb^{2+} ion was absorbed by Whitlockite(WH) dispersed in the suspension. Eco-friendly biomineral was used to remove pollutant to eliminate additional pollution during synthesis and regeneration process. Nano-carbonate hydroxyapatite (CHA) and Whitlockite(WH) were successfully synthesized through wet precipitation method in aqueous solution. Nanoparticle formation was confirmed using XRD analysis. CO_2 absorption and CO_3^{2-} substitution was confirmed using FT-IR analysis and CO_2 absorption behavior during CHA synthesis is ongoing. WH exhibited excellent Pb absorption behavior compared to HAP, which is confirmed using ICP analysis. Phase transformation of WH and HAP after Pb absorption was analyzed with Cs-TEM analysis. Pb absorbed WH was then upcycled to Perovskite Solar Cell(PSC) which showed better performance than PSC from Pb absorbed HAP.

This research has two major impacts. First, released pollutant in the ambient air and water was removed without harsh process. CO_2 was captured via wet precipitation method and Pb ion was absorbed by stirring. Second, removed

pollutant was upcycled to useful material to avoid harsh regeneration process. CHA is utilized as artificial bone material, and Pb absorbed WH was transformed into PbI_2 for precursor of PSC. Consequently, element modified biomineral can successfully remove released pollutant, without harsh regeneration process that can cause additional environmental pollution.

Table of Contents

Abstract	1
-----------------------	----------

Contents	5
-----------------------	----------

Chapter 1. CO₂ absorption via Direct Air Capturing

1.1 Introduction	7
1.2 Experimental methods	
2.2.1 Synthesis of Carbonate Hydroxyapatite (CHA)	9
2.2.2 Nanoparticle characterization	12
1.3 Results and discussions	
2.3.1 Synthesis of CHA and HAP	12
2.3.2 Direct CO ₂ absorption from the air	17
2.3.3 In-vitro study of CHA	19
2.3.4 CO ₃ substitution control	21
1.4 Concluding Remarks	27

Chapter 2. Pb absorption of WH, upcycling to Perovskite Solar Cell

2.1 Introduction	28
2.2 Experimental	
3.2.1 WH and HAP NP Synthesis	31
3.2.2 Nanoparticle Characterization	32
3.2.3 Pb ²⁺ absorption experiment	32
3.2.4 PbI ₂ synthesis	35
3.2.5 PSC fabrication	36
2.3 Results and discussion	
3.3.1 Morphological and structural characterization	38
3.3.2 Absorption performance	44
3.3.3 Characterization of Pb absorbed WH and HAP	56

3.3.4 Pb absorption mechanism of HAP	62
3.3.5 Pb absorption mechanism of WH	70
3.3.6 Reutilization of Pb (PSC)	73
2.4 Concluding Remarks	86

References.....	87
------------------------	-----------

국문초록 (Korean Abstracts)	95
--------------------------------------	-----------

Chapter 1. CO₂ absorption of CHA synthesis, upcycling to artificial bone material

1.1. Introduction

CO₂ emission pollution represents an extremely serious environmental issue in 21st century and enormous efforts were done to deal with problem. Air pollution derived by overuse of fossil fuel caused global warming. CO₂ concentration in the air maintained below 300 ppm over the past 400,000 years, but atmospheric CO₂ level exceeded 400 ppm and continues to increase. Alternative renewable energies are under development to substitute fossil fuel and reduce CO₂ emission, but CO₂ in the air should be retrieved to return to the past.

This massive increase of CO₂ level is mainly due to human activity, and Majority of human CO₂ emission is from fossil fuel combustion, which was taken out of the ground. There are two CO₂ emission sources we must deal with. One is stationary source like combustion gas of factory and chemical waste of industry. CO₂ from stationary source is easy to capture because the source is immovable and CO₂ concentration is relatively high. But when it comes to the other source, the mobile source, is very hard to control because capturing system is hard to be installed on the mobile source, or emission occurs in wide area at low concentration. To solve this problem and lower the CO₂ concentration in the atmosphere, Capturing CO₂ gas directly from

ambient air is also essential as well as suppressing CO₂ release from fossil fuel combustion.

Conventional Direct Air Capturing of CO₂ works in complicated system. Capturing and concentrating process is needed because CO₂ concentration is very low in atmosphere. After capturing CO₂ in the solution, concentrated pallets need calcination to retrieve CO₂ as a form of pure CO₂ gas, which needs high energy. This process is very complicated and causes energy inefficiency, which can lead to additional CO₂ generation.

Research on Direct Air capturing of CO₂ is being done intensively, but there is trouble due to low CO₂ concentration in ambient air. Alkaline and alkaline earth metal, reported as good CO₂ absorbent, were used to capture CO₂ in ambient condition. CaO was used to capture CO₂ from gas. After absorption, Calcite was transformed into carbon monoxide.[1] But it needs higher CO₂ concentration than ambient air, and moreover, needs high temperature to operate. Sodium hydroxide solution successfully absorbed CO₂ directly from the ambient air with 500 ppm.[2] Sodium hydroxide exhibits excellent absorption capacity among other alkaline and alkaline earth metal, but additional harsh regeneration process is needed to retrieve captured CO₂ due to high solubility of sodium carbonate (NaCO₃). Conventional “caustic recovery” reaction uses Calcium hydroxide to precipitate CO₂ into Calcium carbonate, but Calcium carbonate needs very high temperature to release the CO₂ again. This harsh regeneration process should be solved as it causes additional CO₂ emission.

So, CO₂ removing efficiency can be improved via simplification of process after capture. Ca hydroxide is essential in precipitating dissolved CO₂, but Na, instead of Ca is used as an absorber for its superior capturing ability. Promoting capturing ability of Ca is the key to improve the precipitation process. There, we used H₂O₂ to enhance the capturing ability of Ca. H₂O₂ reacts with alkaline and alkaline earth metal hydroxide forming superoxide. [3,4] Anion radical on superoxide then attacks dissolved CO₂ and forms CO₃ ion in the solution, precipitating CaCO₃. Precipitation lowers the concentration of dissolved CO₂, which leads further CO₂ dissolution.

Harsh regeneration was solved by utilizing captured CO₂ directly. Phosphoric acid was introduced in the CO₂ captured solution to synthesize Carbonate Hydroxyapatite. Synthesized CHA exhibited good biocompatibility, showing possible application to cure for bone illnesses.

Here, we synthesized Carbonate substituted hydroxyapatite as a product of CO₂ capture which is eco-friendly biomaterial existing in human body. CHA successfully captured CO₂ directly from ambient air during synthesis. CO₃²⁻ substituted PO₄³⁻ forming B-type CHA. CO₂ capturing capacity and kinetics is under further research.

1.2. Experimental

1.2.1 Synthesis of Carbonate Hydroxyapatite

Carbonate hydroxyapatite (CHA) was synthesized using wet precipitation method. First, 100ml of 1M $\text{Ca}(\text{OH})_2$ aqueous solution was vigorously stirred and sonicated for 5 minutes to make the suspension uniform. Then, 100ml of H_2O_2 solution of desired concentration was added. After another 5 minutes, 100ml of 0.6M H_3PO_4 aqueous solution was added. The precipitates were aged for 8 hours and then collected using centrifuge. The precipitants were lyophilized overnight. The scheme of this precipitation process was shown at figure 1.1. All procedures were carried out under controlled environment at ambient condition (500ppm of CO_2 concentration), but temperature (30, 40°C) and H_2O_2 concentration were adjusted to examine the effect on capture and synthesis.

For the comparison between synthesized CHA and hydroxyapatite (HAP), HAP was also synthesized using wet precipitation. 500ml of 1M $\text{Ca}(\text{OH})_2$ aqueous solution and 500 ml of 0.6M H_3PO_4 aqueous solution were prepared. The $\text{Ca}(\text{OH})_2$ solution was sonicated and stirred for 30 minutes. Then, H_3PO_4 solution was added to the $\text{Ca}(\text{OH})_2$ solution with a constant rate, 12.5ml/min, using digital burette. After the 24 hour-aging time, the precipitates were collected and dried in same way as mentioned above.

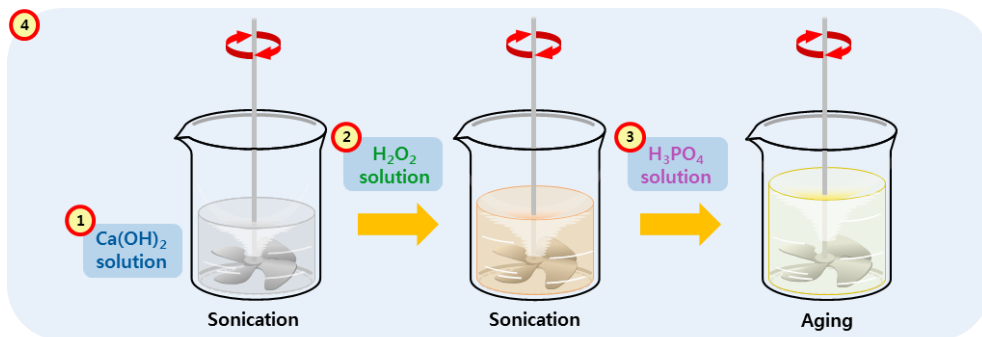


Figure 1.1 Carbonate hydroxyapatite (CHA) was synthesized using wet precipitation method. First, 100ml of 1M Ca(OH)_2 aqueous solution was vigorously stirred and sonicated for 5 minutes to make the suspension uniform. Then, 100ml of H_2O_2 solution of desired concentration was added. After another 5 minutes, 100ml of 0.6M H_3PO_4 aqueous solution was added. The precipitates were aged for 8 hours and then collected using centrifuge. The precipitants were lyophilized overnight.

1.2.2 Nanoparticle Characterization

XRD patterns were obtained by an X-ray diffractometer (D8 Advance, 2020 Bruker, Germany) operating at a power of 3 kW (40 kV, 40 mA) with a Cu K α source ($\lambda = 1.541 \text{ \AA}$). Fourier transform infrared spectroscopy (FT-IR) spectra were obtained using a FT-IR spectrometer (Nicolet iS10, Thermoscientific).

1.3 Results and Discussions

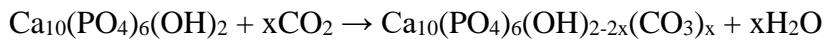
1.3.1 Characterization of synthesized CHA and HAP

CHA and HAP were synthesized via simple precipitation-induced crystallization in a calcium hydroxide solution by addition of a phosphate solution; H₂O₂ solution was added before phosphate solution, which aided in forming a CHA structure.

The XRD pattern of our synthesized CHA. It is possible to verify the spectrogram aspect of synthesized CHA with JSPDS. XRD spectrum of synthesized HAP well matches to crystal data of (HAP JCPDS 01-074-9761). XRD pattern of synthesized CHA is in good agreement with the crystal structure data of Carbonate Hydroxyapatite(JSPDS 01-075-3727) showing distinct peaks to hydroxyapatite. Peak of (112) plane was generated

at 32 degree and peaks of (121) and (300) plane shifted toward lower degree, showing decreased ratio of c/a lattice as a result of CO_3^{2-} doping.

CO_3^{2-} anion can substitute into two different sites in the HAP.[5] Type A is Apatite which carbonate substitutes hydroxyl group. A type is synthesized at high temperature because detaching hydroxyl group requires high energy.



Type B, on the other hand, is Apatite which carbonate substitutes phosphate group. Carbonate Apatite synthesized in the body is B type because it has low energy barrier and good surface affinity with osteoblastic cells. We expect B type CHA will be synthesized as experiment goes at low temperature.



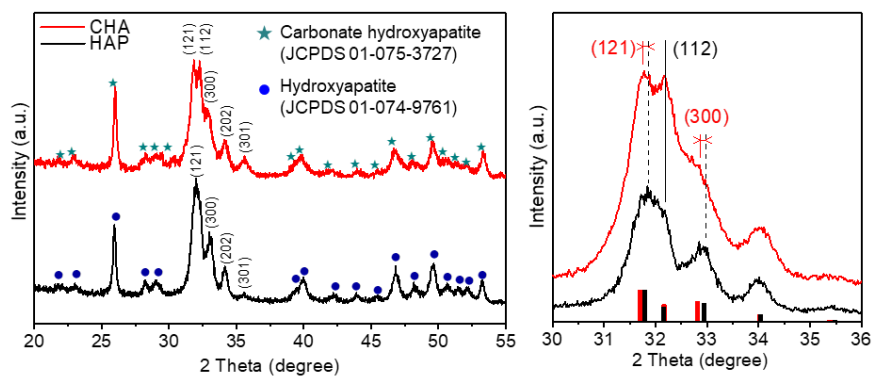


Figure 1.2 XRD spectrum of synthesized Carbonate hydroxyapatite (CHA) and Hydroxyapatite (HAP).

Morphology of HAP and CHA NPs was examined with Field Emission Scanning Electron Microscopy (FESEM). HAP without Carbonate showed rice like morphology, whereas CHA exhibits flower like shape. XRD and SEM result shows there's no other phases except desired apatite, therefore we confirmed that we successfully synthesized CHA via wet precipitation method, without using precursor containing Carbonate.

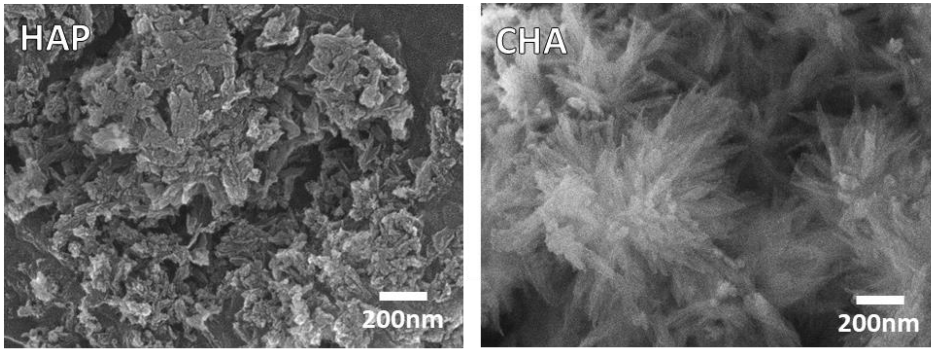


Figure 1.3 FE-SEM images of synthesized Hydroxyapatite (HAP) and Carbonate hydroxyapatite (CHA). HAP without Carbonate showed rice like morphology, whereas CHA exhibits flower like shape.

1.3.2 Direct CO₂ absorption from the air

As CHA was successfully synthesized with precursor containing CO₃, it is obvious that CO₃²⁻ was derived from air. Closed system was used To confirm the origin of CO₃. Closed system was made of acryl box with one sided door and sealable hole for CO₂ detection. There, we put 100ml beaker for CHA synthesis, and the suspension was vigorously stirred by stirrer from outside. Gas mixer using mass flow controller(MFC) was used to make the initial CO₂ concentration of the box 500 ppm, same as ambient air. Beaker with suspension was inserted into the box after all precursors were introduced. The amount of CO₂ continuously decreased as the reaction progressed but slowed down as saturated to 0 ppm. It's because the box is closed system. It took only 1 hour to consume all CO₂ in the box which shows high absorption kinetics of the suspension. Further experiment is under work to determine the capacity and kinetics during the CHA synthesis.

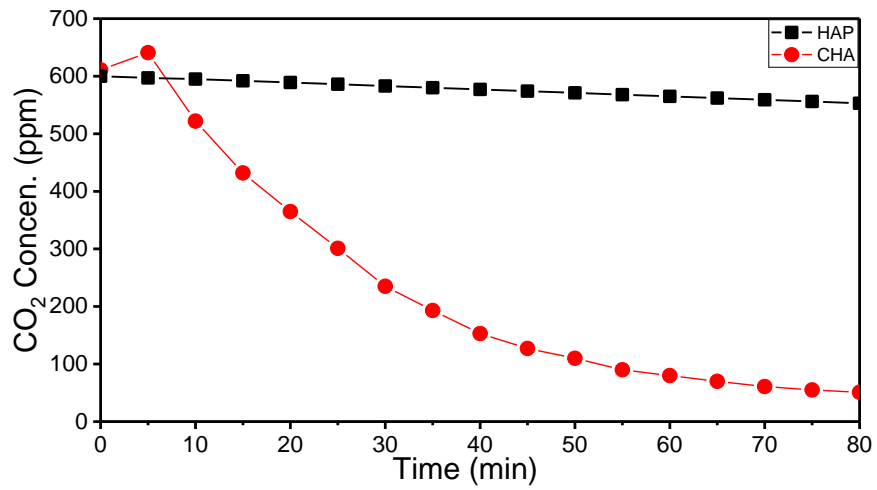


Figure 1.4 CO₂ concentration time profile inside the box after the beaker with CHA synthesis suspension is inserted.

1.3.2 In-vitro study of CHA

In-vitro study of synthesized CHA and HAP was conducted to examine the biocompatibility of the materials. Carbonate doped Apatite showed enhancement in proliferation, compared to Control group and HAP. This means that cells grow and multiply better on the CHA.

In proliferation test, CHA exhibited similar proliferation of hADSCs to that of HAP and β -TCP. qPCR Analysis was also conducted to see the osteogenic differentiation. This analysis is to see how cells binds on the pallet, and activity of osteoblast cell which makes bone material. RUNX2, plays a cell proliferation regulatory role in bone formation, and OSX accelerates the proliferation of osteoprogenitor at the next stage, which is the precursor of osteoblast cell. OCN is a protein secreted from bone after bone formation.

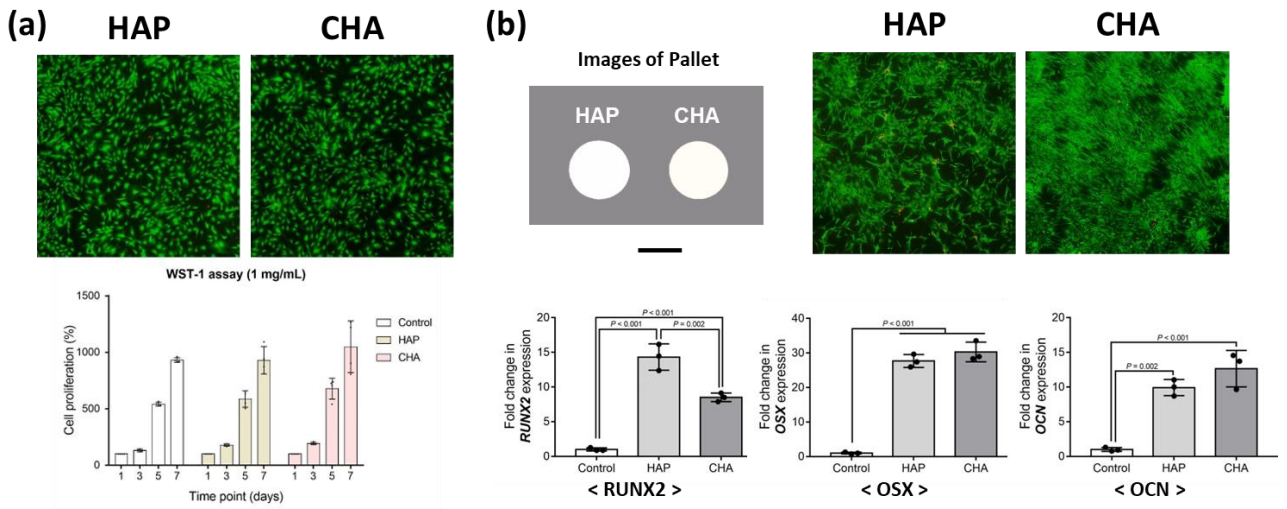


Figure 1.2 In-vitro study of CHA and HAP. (a) proliferation test results and (b) real-time qPCR analysis results of CHA and HAP.

1.3.3 CO₃ substitution control

Temperature and H₂O₂ concentration were controlled to vary the CO₃²⁻ substitution rate in CHA. Crystallinity showed little difference in XRD spectrum according to temperature and H₂O₂ concentration. But Morphological difference was found when synthetic temperature varied. Rice like ellipsoidal shape was formed at 30°C, whereas flower like shape was formed at 40°C.

Figure 1.4 shows FT-IR spectrum of synthesized CHA through wet precipitation method. The spectrum indicated that our CHA has CO₃ substitution. The peaks appearing at wave number values of 873, 1420, and 1482 cm⁻¹ demonstrated that the carbonate ion substitution in CHA lattice. The broad band appeared at 1638 and 3440 cm⁻¹ indicate adsorbed H₂O in the materials. The band of structural OH which appears at around 3565 cm⁻¹ is scarcely visible because the band at 3440 cm⁻¹ which is due to adsorbed water overlaps the weak band of structural OH. In addition, we further analyze our FT-IR spectrum to check whether our CHA is A-type carbonate hydroxyapatite, OH ion site is substituted by CO₃ ion, or B-type hydroxyapatite, PO₄ ion site is substituted by CO₃ ion. According to reported result⁷¹, our CHA can be considered as B-type. However, it cannot entirely exclude the possibility of A-type carbonate apatite fractions. The fraction of A-type and B-type could be calculated through the peak area

comparison⁷². Because the typical peak of A-type CHA is 880 cm^{-1} and that of B-type is 872 cm^{-1} , the presence of CO_3 substituting in the OH site or PO_4 can be evaluated by the peak area ratio¹. The calculated A/B ratio of our CHA is about 0.4. Therefore, our CHA can be regarded AB-type carbonate hydroxyapatite like natural bone.

CO_3^{2-} peak of CHA showed difference according to H_2O_2 concentration. CO_3^{2-} peaks at 1420 , and 1482 cm^{-1} increased as H_2O_2 concentration increases. Temperature didn't show significant affect to the amount of CO_3^{2-} substitution.

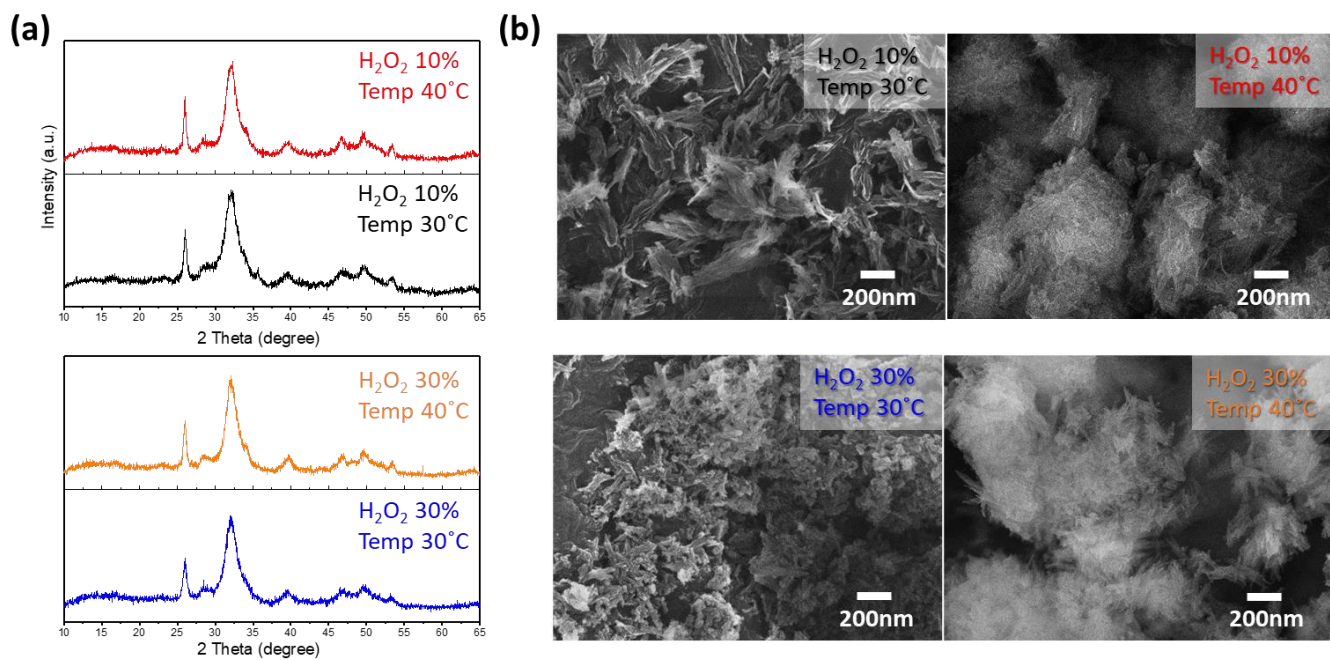


Figure1.3 Characterization of CHA and HAP according to temperature and H₂O₂ concentration.

Figure 1.4 shows FT-IR spectrum of synthesized CHA through wet precipitation method. The spectrum indicated that our CHA has CO_3 substitution. The peaks appearing at wave number values of 873, 1420, and 1482 cm^{-1} demonstrated that the carbonate ion substitution in CHA lattice. The broad band appeared at 1638 and 3440 cm^{-1} indicate adsorbed H_2O in the materials. The band of structural OH which appears at around 3565 cm^{-1} is scarcely visible because the band at 3440 cm^{-1} which is due to adsorbed water overlaps the weak band of structural OH. In addition, we further analyze our FT-IR spectrum to check whether our CHA is A-type carbonate hydroxyapatite, OH ion site is substituted by CO_3 ion, or B-type hydroxyapatite, PO_4 ion site is substituted by CO_3 ion. According to reported result⁷¹, our CHA can be considered as B-type. However, it cannot entirely exclude the possibility of A-type carbonate apatite fractions. The fraction of A-type and B-type could be calculated through the peak area comparison⁷². Because the typical peak of A-type CHA is 880 cm^{-1} and that of B-type is 872 cm^{-1} , the presence of CO_3 substituting in the OH site or PO_4 can be evaluated by the peak area ratio¹. The calculated A/B ratio of our CHA is about 0.4. Therefore, our CHA can be regarded AB-type carbonate hydroxyapatite like natural bone.

CO_3^{2-} peak of CHA showed difference according to H_2O_2 concentration. CO_3^{2-} peaks at 1420, and 1482 cm^{-1} increased as H_2O_2 concentration increases.

Temperature didn't show significant affect to the amount of CO_3^{2-} substitution.

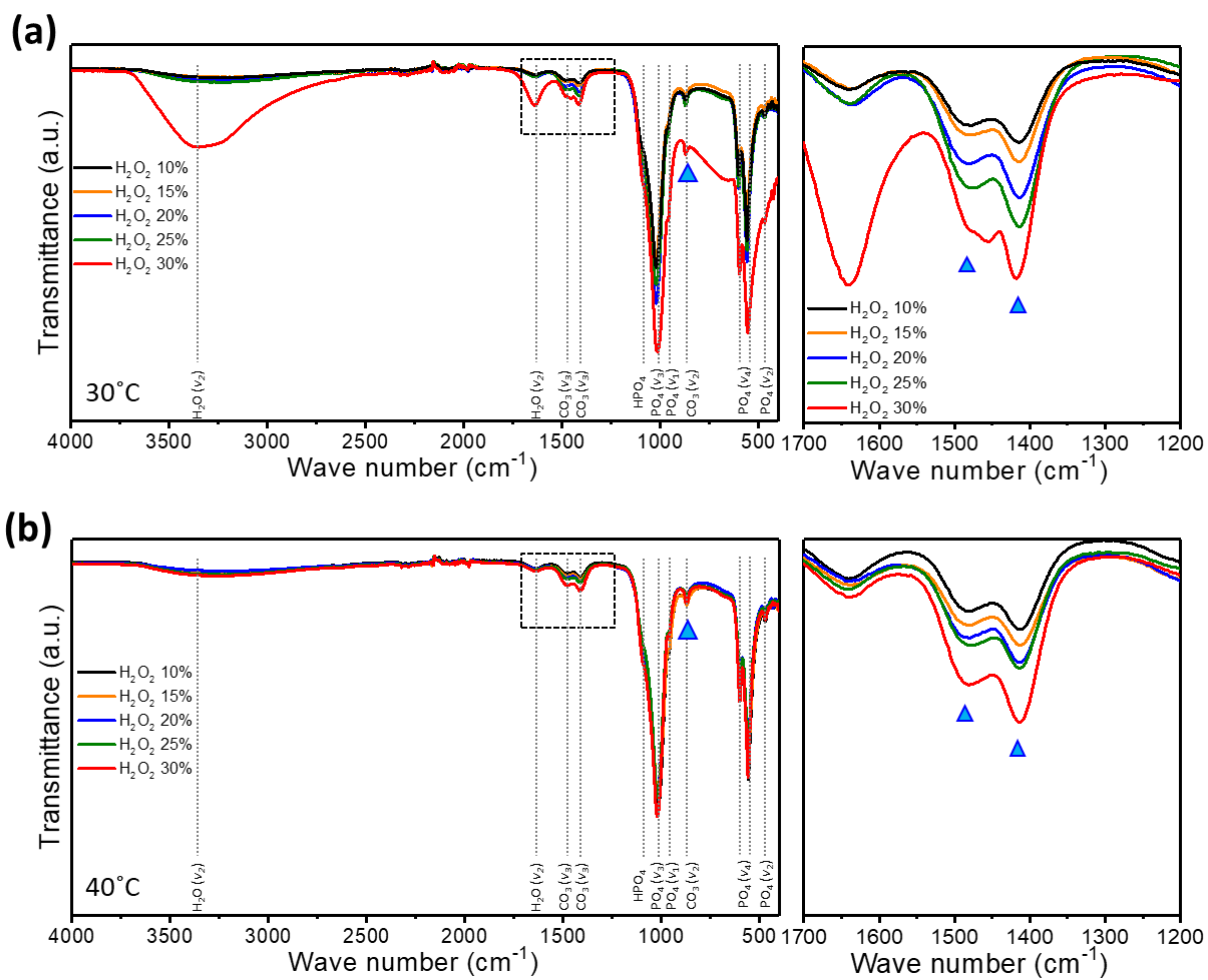


Figure 1.4 FT-IR spectrum of CHA according to temperature and H₂O₂ concentration.

1.4 Concluding Remarks

In this research, Ca(OH)_2 solution can absorb CO_2 in the ambient air effectively in assist of H_2O_2 , and amount of CO_3^{2-} substitution into hydroxyapatite can be controlled by H_2O_2 concentration.

In the future, CO_2 absorption kinetics and capacity will be examined to understand the mechanism of CO_2 absorption behavior of Ca(OH)_2 . Structural deformation of CHA by CO_3^{2-} substitution will be analyzed with SAED patterns of Cs-TEM.

Chapter 2. Pb absorption of WH, upcycling to Perovskite Solar Cell

2.1. Introduction

Although Global warming is an urgent issue, people show little movements on reducing CO₂ emission and development and using renewable energy. Even the old environmental pollution is not yet completed. Especially when it comes to Heavy metal pollution, well know for decades, it causes an extremely serious environmental pollution over and over. Aquatic resources in the nature supports all the creatures on the planet. Overall, activity of life occurs based on water, as over half of the cells are consisted of water. Heavy metal ions dissolved in water can easily spread and infiltrate living organism. Absorbed heavy metal in the body does not easily degraded itself, and moreover tends to bioaccumulate.

Especially when it comes to lead(Pb), Pb is more favorable to apatite forming Hydroxy Pyromorphite(HPy) than Hydroxyapatite which is consisted of Ca. HPy is more stable than HAP, because HPy is more thermodynamically favorable. It substitutes HAP originally consisting human bone, decreases stability of human bone as mechanical strength is weaker than HAP, consist of Ca. Thus, Pb concentration is restricted by the US Environmental Protection Agency to values below 0.015 mg L⁻¹ in drinking water.[6]

Pb pollution once seemed to disappear as heavy metal pollution aroused people's attention. But demand of Pb stayed high and even increased as lead battery demand increased as development of electric mobile transportation got intensive. Moreover, Over the last decade, perovskite solar cells (PSCs) have rapidly achieved a power conversion efficiency (PCE) of 25.7%, and, therefore, they represent the most promising candidates for next-generation renewable energy conversion devices. Although PSC is getting attention as one of the promising renewable energy device, Pb, which is main component of PSC, is one of the most difficult obstacle to overcome. Although researches are intensively done to manufacture PSC without Pb, it seem hard to be achieved in short time. So, processes of PSC should be warranted as Pb leakage-free to realize and commercialize PSC for renewable energy. But countermeasure requires against Pb leakage, using efficient Pb absorbents obtained from environmentally friendly materials.[7–11]

Several approaches have been attempted to remove Pb from wastewaters using various materials, such as activated carbon, metal oxides (Fe_2O_3 , MnO_2 , and $\gamma\text{-Al}_2\text{O}_3$) [12–14], hybrid composites (chitosan/ Fe_3O_4 , graphene oxide/ Fe_3O_4 -*g*-polymethacrylamide) [15,16], carbon nanotubes, and hydroxyapatite (HAP, $\text{Ca}_{10}(\text{PO}_4)_6(\text{OH})_2$).[17–20] In particular, biomineral HAP has attracted substantial attention owing to its limited residue production, biodegradability, and high absorption capacity for heavy metals including Pb. HAP has shown a higher Pb^{2+} absorption capacity than other

absorbents, equal to 1269.01 mg g⁻¹. [21] In addition, Park et al have recently reported the used of iron-incorporated HAP for PSC recycling. [6]

Capability of various metal cation substitution in hydroxyapatite has pushed towards an extensive use maintaining its inorganic phase of biomineral. Various metal cations like Strontium(Sr), Zinc(Zn), Manganese(Mn) substitutes into cation site, resulting in various distinct effects due to structure distortion. [22] Sr incorporated HAP at low concentration increases solubility and lowers stability. Moreover, released Sr significantly enhances osteoblasts activity, and inhibits osteoclast activity. Mn inhibits crystallinity of HAP impacting on the apatite bioactivity.

In case of Pb, Pb substituted HAP forms pyromorphite which shows lower solubility due to higher crystallinity and stability. This material exhibited high absorption capacity and fast kinetics, removing Pb²⁺ ions completely from a waste solution and proving to be a promising solution for PSC recycling. However, the Pb-absorbed HAP still contained a high amount of residual Ca²⁺ ions, which may affect the purity of recycled PbI₂. An excess of over 0.5% Ca²⁺ ions in PbI₂ could decrease the solar cell efficiency by generating crystal phase impurity. [23,24] In addition, the residual Ca²⁺ ions in the perovskite precursor often lead to defects in perovskite films, leading to low PSC performance.

Here, for the first time, we synthesized whitlockite (WH, Ca₁₈Mg₂(HPO₄)₂(PO₄)₁₂), the second most abundant biomineral in human hard tissues, to use as a novel Pb²⁺ absorbent. Surprisingly, WH exhibited

an unexpected Pb^{2+} absorption capacity of 2339 mg g^{-1} , which is the highest value reported for Pb^{2+} absorbents so far. In addition, WH nanoparticles (NPs) were completely transformed into single-crystal Pb^{2+} compounds without other metal cations, leading to a high PbI_2 purity during the recycling process. Consequently, the recycled PbI_2 powder used as a perovskite precursor showed a PCE of 19.00%, similar to that of commercial PbI_2 (purity = 99.99%).

2.2. Experimental

2.2.1 WH and HAP NP Synthesis

A wet precipitation method was used to synthesize WH ($\text{Ca}_{18}\text{Mg}_2(\text{HPO}_4)_2(\text{PO}_4)_{12}$) and HAP ($\text{Ca}_{10}(\text{PO}_4)_6(\text{OH})_2$). For the former, 0.77 M calcium hydroxide and 0.23 M magnesium hydroxide was added to 500 mL deionized water and homogeneously mixed via sonication and overhead stirring. After 10 min, the solution was heated to 80 °C under vigorous stirring. Then, 500 mL of a 0.95 M phosphoric acid solution was added dropwise at a rate of 12.5 mL min^{-1} using a digital burette (Metrohm 876, Dosimat Plus). The suspension was aged for 24 h, and the precipitate was pressure filtered and lyophilized to prevent agglomeration. HAP was synthesized via a similar method with identical starting materials: 500 mL of 1 M calcium hydroxide was vigorously stirred with an overhead stirrer during sonication; then, 500 mL of a 0.3 M phosphoric acid solution was

added dropwise at a rate of 12.5 mL min⁻¹ using a digital burette. The suspension was aged for 24 h while stirring continuously. The precipitate was pressure filtered and lyophilized. Annealing process was done at 400°C for 6 to observe the effect of crystallinity on Pb absorption.[25]

2.2.2 Nanoparticle Characterization

XRD patterns were obtained by an X-ray diffractometer (D8 Advance, 2020 Bruker, Germany) operating at a power of 3 kW (40 kV, 40 mA) with a Cu K α source ($\lambda = 1.541 \text{ \AA}$). ICP analysis was carried out on an ICP-atomic emission spectrometer (OPTIMA 8300, Perkin-Elmer, USA). TEM images were obtained using a Cs-corrected TEM (JEM-ARM200F, Cold FEG, JEOL Ltd, Japan).

2.2.3 Pb²⁺ absorption experiments

A stock solution of Pb(NO₃)₂ was prepared and diluted to the desired concentrations, ranging from 10 ppm to 3000 ppm. Then, HAP or WH (1 g L⁻¹) was introduced into the Pb²⁺ solutions, followed by sonication within 2 min to prevent agglomeration. The solution was kept under stirring at 200 rpm, and the absorption experiments were performed at ambient conditions. The precipitates were collected through centrifugation and lyophilized for

XRD analysis. The solutions were filtered using a cellulose acetate membrane with a 0.22 μm pore size for ICP analysis.

Pb^{2+} solutions at various concentrations were prepared for the absorption experiments using $\text{Pb}(\text{NO}_3)_2$ in deionized water. The synthesized HAP and WH were introduced at 1g L^{-1} into these Pb^{2+} solutions and sonicated for less than 2 min. The residual Pb^{2+} ion concentration was determined by ICP analysis.

The absorption capacities (the amount of Pb^{2+} ions absorbed per specific quantity of absorbent, q_t) and percentage removals (Removal(%)) were calculated using Eq. S1 and S2, respectively:

$$q_t = (C_0 - C_t)V/m \quad (\text{S1})$$

$$\text{Removal}(\%) = (C_0 - C_t)/C_0 \quad (\text{S2})$$

where C_0 and C_t are, respectively, the initial and remaining concentrations of Pb; V is the volume of Pb^{2+} solution; and m is the mass of the absorbents.

In the experiments carried out to determine the absorption isotherms, the absorbents were introduced in 20 mL of Pb^{2+} solutions at various concentrations, ranging between 10 and 3000 ppm, for 2 h. The solutions were analyzed via inductively couple plasma atomic emission spectroscopy, and the results were then fitted according to the Langmuir and Freundlich isotherm models. The Langmuir isotherm is defined by Eq. S3:

$$q_e = \frac{q_m K_L C_e}{1 + K_L C_e} \quad (\text{S3})$$

where q_e is the amount of absorbed Pb^{2+} per specific amount of absorbent, q_m is the maximum amount of Pb^{2+} ions required to form a monolayer, C_e is the equilibrium concentration of Pb^{2+} in the solution, and K_L is the Langmuir constant. Following Eq. S4, the linear plot of C_e/q_e vs. C_e was used to evaluate q_m and K_L .

$$C_e/q_e = 1/(K_L q_m) + C_e/q_m \quad (S4)$$

The Freundlich isotherm is given by Eq. S5:

$$q_e = K_F C_e^{1/n} \quad (S5)$$

where q_e is the amount of absorbed Pb^{2+} at equilibrium, K_F is the Freundlich constant or an approximate indicator of the absorption capacity, C_e is the final Pb^{2+} concentration after absorption, and $1/n$ is a function of the adsorption strength (n is the adsorption intensity). K_F and $1/n$ can be obtained from the following linear plot (Eq. S6):

$$\log q_e = \log K_F + (\log C_e)/n \quad (S6)$$

In the adsorption kinetics experiments, 1 g L⁻¹ adsorbent was introduced in 50 mL of a Pb^{2+} solution with a concentration of 1000 ppm. Samples were extracted from the same solution at desired contact times of up to 90 min. The experimental data were fitted according to the pseudo-first order (PFO) and pseudo-second order (PSO) kinetics models.

PFO kinetics are expressed by Eq. S7:

$$\log(q_e - q_t) = \log q_e - (k_1 t)/2.303 \quad (S7)$$

where q_e is the absorption capacity at equilibrium, q_t is the absorption capacity at contact time t , and k_1 is the PFO constant. Eq. S7 may be expressed differently, as in Eq. S8:

$$q_t = q_e(1 - \exp(-k_1 t)) \quad (\text{S8})$$

PSO kinetics are represented by Eq. S9:

$$t/q_t = 1/(k_2 q_e^2) + t/q_e \quad (\text{S9})$$

where q_e is the absorption capacity at equilibrium, q_t is the absorption capacity at contact time t , and k_2 is the PSO constant. Eq. S9 may also be given as Eq. S10:

$$q_t = q_e \frac{k_2 q_e t}{1 + k_2 q_e t} \quad (\text{S10})$$

The 4-(2-pyridylazo)-resorcinol (PAR) pigment was used to evidence different solution colors according to Pb^{2+} concentration to visualize the Pb^{2+} absorption ability. PAR was introduced in the Pb^{2+} solution at the desired time.

2.2.4 PbI_2 synthesis

The experiments involving the synthesis of PbI_2 from the Pb^{2+} -containing absorbents were conducted to investigate the possible reusability of the materials. To synthesize PbI_2 , the Pb-apatite resulted from Pb^{2+} absorption was dissolved in solutions of HNO_3 and KI until no more precipitation was observed. The yellow precipitate was washed with deionized water and

centrifuged multiple times until a pH value greater than 5 was measured. A PSC was fabricated using this powder as well as the commercial chemical for comparison.

2.2.5 PSC fabrication

The patterned indium tin oxide (ITO) substrates were cleaned sequentially using detergent, deionized water, acetone, and ethanol in an ultrasonic bath for 10 min. The substrates were treated with UV-ozone to enhance the wettability and remove organic contaminants.

27 mg $\text{SnCl}_2 \cdot 2\text{H}_2\text{O}$ (Aldrich, > 99.995 %) in 3156 mg ethanol (anhydrous, Decon Laboratories Inc.) was dissolved in a tin colloid (Alfa Aesar, 15 %) solution diluted at a 1:4 ratio and then filtered before use. Then, 20 μL of an SnO_2 solution was spin-coated on the UV-ozone-treated substrate at 4000 rpm for 30 s, followed by annealing at 100 °C for 10 min on a hot plate. After the substrate had cooled to room temperature, the spin-coating process was repeated to enhance the coverage of the SnO_2 layer. The film was annealed at 150 °C for 5 min and 180 °C for 120 min. The $\text{SnO}_2/\text{ITO}/\text{glass}$ system was treated with UV-ozone before coating the perovskite films.

A perovskite precursor solution was prepared as follows. Dimethylformamide and dimethyl sulfoxide were mixed in a 7:3 ratio to obtain 1 mL solution. Next, 0.52 M methylammonium chloride, 0.08 M lead bromide, 0.08 M methylammonium bromide, 0.08 M cesium iodide, 1.45 M

formamidinium iodide, and 1.53 M lead iodide were added to the solution. The latter was spin-coated on the ITO substrate at 5000 rpm for 25 s, and anisole was dropped 18 s after spin-coating. The intermediate phase film was then heated to 150 °C for 10 min. Subsequently, spiro-MeOTAD was spin-coated onto the perovskite film at 3000 rpm for 30 s by dropping 25 μL of the solution, which had been prepared by dissolving 50.4 mg spiro-MeOTAD in a mixture composed by 700 μL chlorobenzene 20.2 μL of 4-tert-Butylpyridine, and 12.3 μL of a lithium bis(trifluoromethanesulfonyl)imide solution (720 mg mL^{-1} in acetonitrile).

The photovoltaic properties of the PSCs were measured using a potentiostat (CHI 600D, CH Instruments) under 1-sun illumination generated by a solar simulator (Newport Oriel Solar 3A Class, 64023A). The light intensity was adjusted using a standard Si solar cell (Oriel, VLSI standards). The J–V characteristics for all devices were measured at a voltage scan rate of 0.1 V s^{-1} . The PSCs without any pre-conditioning, such as applied bias voltage or light soaking, were covered with a metal mask (0.14 cm^2) to control the active area precisely during the measurements. The EQE was tested using a specially designed system named Enlitech under the AC mode (frequency = 133 Hz) without bias light. The steady-state power conversion efficiency was calculated from the stabilized photocurrent density at a constant bias voltage.

2.3. Results & discussion

2.3.1 Morphological and structural characterization

HAP and WH NPs were synthesized via simple precipitation-induced crystallization in a calcium hydroxide solution by dropwise addition of a phosphate solution; the first solution also contained magnesium hydroxide, which aided in forming a WH structure.[25] Figure 2.1 displays the schematic crystal structure of the synthesized HAP and WH, drawn using the software CrystalMaker (CrystalMaker Software Ltd., Oxford, England (www.crystallmaker.com)) based on previously reported databases of the crystal structures of WH and HAP.[25,26]

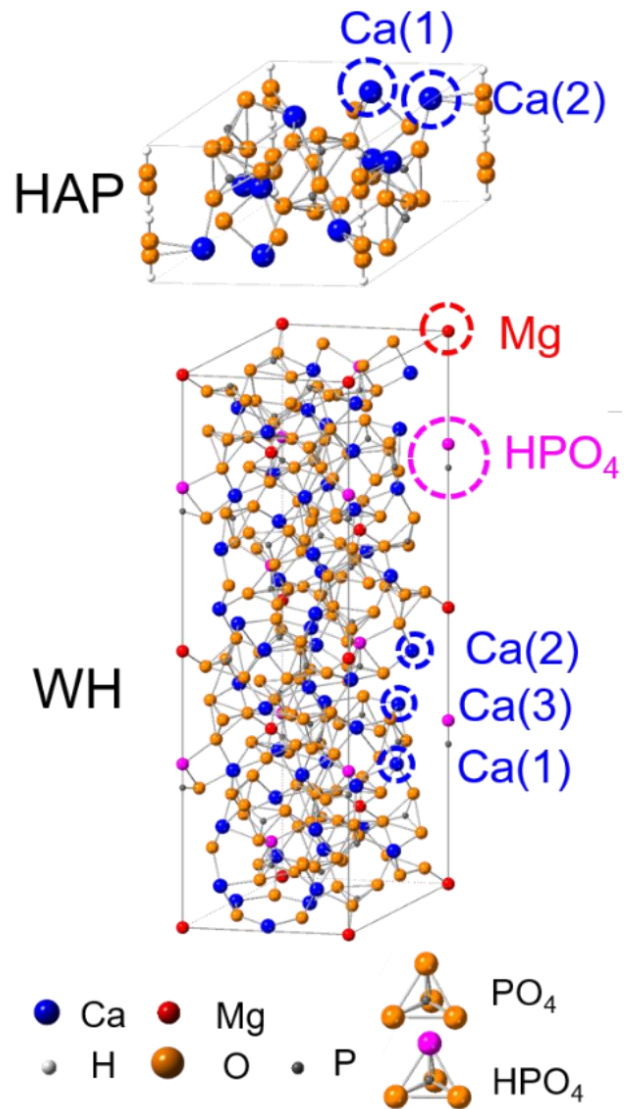


Figure 2.1. Synthesized hydroxyapatite (HAP: $\text{Ca}_{10}(\text{PO}_4)_6(\text{OH})_2$) and whitlockite (WH: $\text{Ca}_{18}\text{Mg}_2(\text{HPO}_4)_2(\text{PO}_4)_{12}$) nanoparticles. Crystal structure in HAP and WH.

HAP consists of two different Ca^{2+} sites: triangular $\text{Ca}^{2+(1)}$ sites are surrounded by three PO_4^{3-} groups, whereas quasi-octahedral $\text{Ca}^{2+(2)}$ sites are surrounded by four PO_4^{3-} groups and two OH^- groups. WH shows a unique structure with three different Ca^{2+} sites and one Mg^{2+} site: the $\text{Ca}^{2+(1)}$ sites are directly bonded to three PO_4^{3-} , where one of these is connected to an Mg^{2+} atom; the $\text{Ca}^{2+(2)}$ sites are surrounded by three PO_4^{3-} groups and one HPO_4^{3-} group; each $\text{Ca}^{2+(3)}$ atom also adjoins three PO_4^{3-} groups; finally, the Mg^{2+} site is located at the center of a PO_4^{3-} octahedron. Figure 2.2 shows the X-ray diffraction (XRD) patterns of the synthesized HAP and WH. HAP has a hexagonal ($\text{P6}_3/\text{m}$) structure with lattice parameters $a = 9.4176 \text{ \AA}$ and $c = 6.8814 \text{ \AA}$, whereas WH presents a rhombohedral (R3c) structure with lattice parameters $a = 10.35 \text{ \AA}$ and $c = 37.085 \text{ \AA}$; the structural data obtained from the XRD patterns are in good agreement with the theoretical parameters.

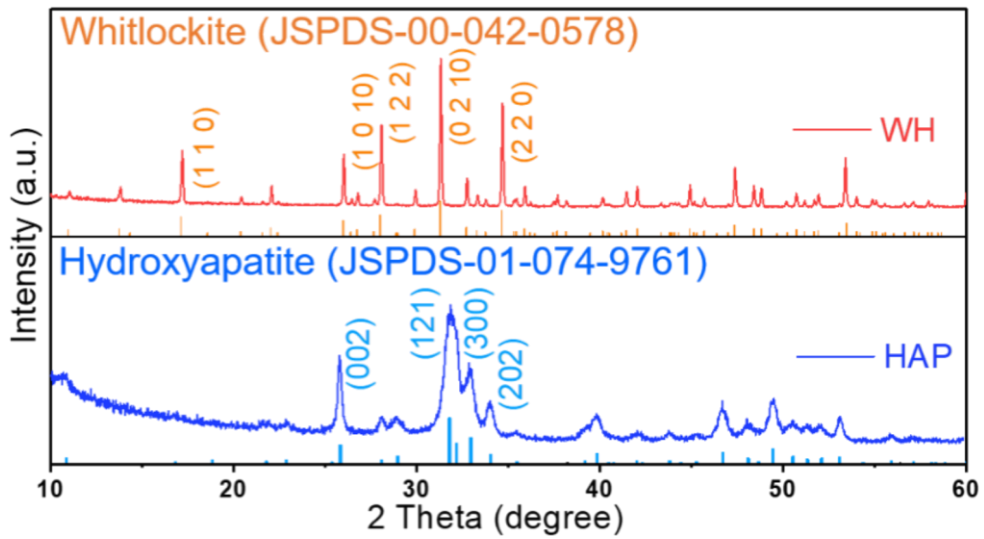


Figure 2.2. Synthesized hydroxyapatite (HAP: $\text{Ca}_{10}(\text{PO}_4)_6(\text{OH})_2$) and whitlockite (WH: $\text{Ca}_{18}\text{Mg}_2(\text{HPO}_4)_2(\text{PO}_4)_{12}$) nanoparticles. X-ray diffraction patterns of the synthesized WH and HAP.

HAP NPs presented a homogeneous ellipsoidal shape with a size of approximately 123.87 ± 29.38 nm and d-spacing of 2.844 \AA , corresponding to the (112) plane of HAP, as shown in Figure 2.3. (a) WH NPs exhibited a rhombohedral morphology with a size of 53.78 ± 4.79 nm and d-spacing of 2.861 \AA , corresponding to the (2 0 10) plane of WH. Both NP types showed ordered arrays of spots in the SAED pattern of HAP (inset of Figure 2.3 (c)) and the FFT mode of WH (inset of Figure 2.3 (b)), indicating a high crystallinity and the absence of defects.

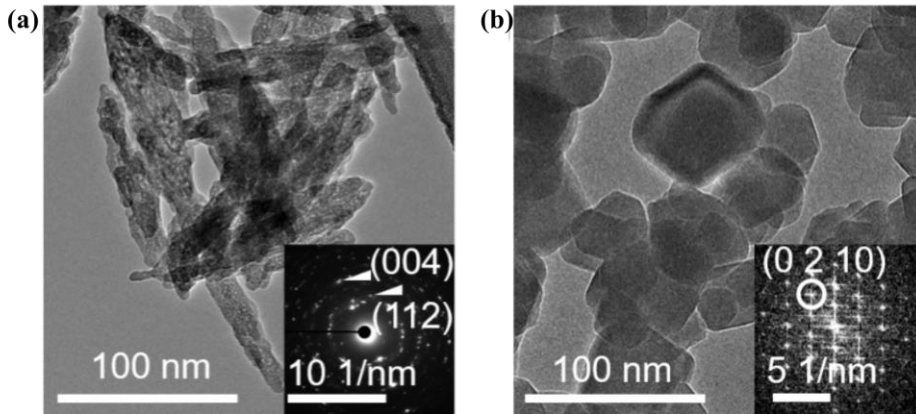


Figure 2.3. Synthesized hydroxyapatite (HAP: $\text{Ca}_{10}(\text{PO}_4)_6(\text{OH})_2$) and whitlockite (WH: $\text{Ca}_{18}\text{Mg}_2(\text{HPO}_4)_2(\text{PO}_4)_{12}$) nanoparticles. (a) High-resolution transmission electron microscopy (HR-TEM) and selected area electron diffraction (SAED) pattern (inset) of HAP. The d-spacing value in the SAED pattern is in good agreement with the crystal structure data of HAP (JCPDS 01-074-9761). (b) HR-TEM and fast Fourier transform mode (inset) of WH. The d-spacing value in the SAED pattern is in good agreement with the crystal structure data of WH (JCPDS-00-042-0578).

2.3.2 Absorption performance

Figure 2.4 shows the Pb^{2+} removal performance of HAP and WH NPs in a 4.83 mM $\text{Pb}(\text{NO}_3)_2$ aqueous solution (Pb^{2+} concentration: 1000 ppm) as function of time. Surprisingly, any remaining Pb^{2+} ion was not detected in WH NPs introduced solution; however, HAP NPs exhibited a removal efficiency of only 16%. In addition, the 4-(2-pyridylazo)-resorcinol (PAR) dye was used as a colorimetric reagent for Pb^{2+} ions to better highlight and compare the different removal performances of HAP and WH, as shown in the inset of Figure 2.4.[27] The solution of WH NPs containing PAR underwent a drastic change in color from red to light yellow over 30 min. In contrast, the initial red color in the PAR-containing solution of HAP NPs persisted even after 60 min. These observations are consistent with the determination of Pb^{2+} concentration carried out via inductively-coupled plasma (ICP) atomic emission spectroscopy.

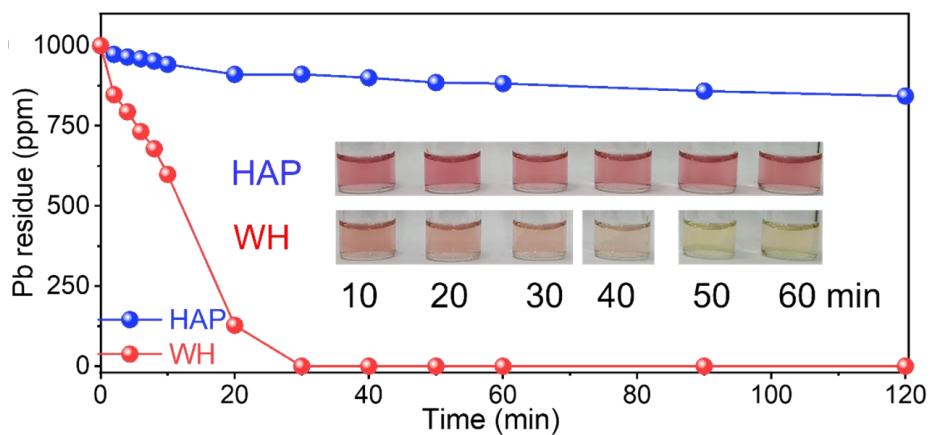


Figure 2.4 Pb²⁺ absorption by as-synthesized hydroxyapatite (HAP) and whitlockite (WH) (inset displays the color change of Pb²⁺ solutions with 4-(2-pyridylazo)-resorcinol as a function of time).

To confirm the Pb^{2+} removal mechanism for WH and HAP, the absorption kinetics and isotherms were investigated; these are plotted in Figure 2.5 and 2.6. The absorption kinetics of HAP and WH were calculated with a befitting model of pseudo-second order: the obtained correlation coefficients R^2 of 0.974 and 0.992, respectively, compared to those obtained for the pseudo-first order (0.932 and 0.926), indicated that Pb^{2+} absorption took place via a chemisorption process rather than physisorption (Figure 2.7).[28]

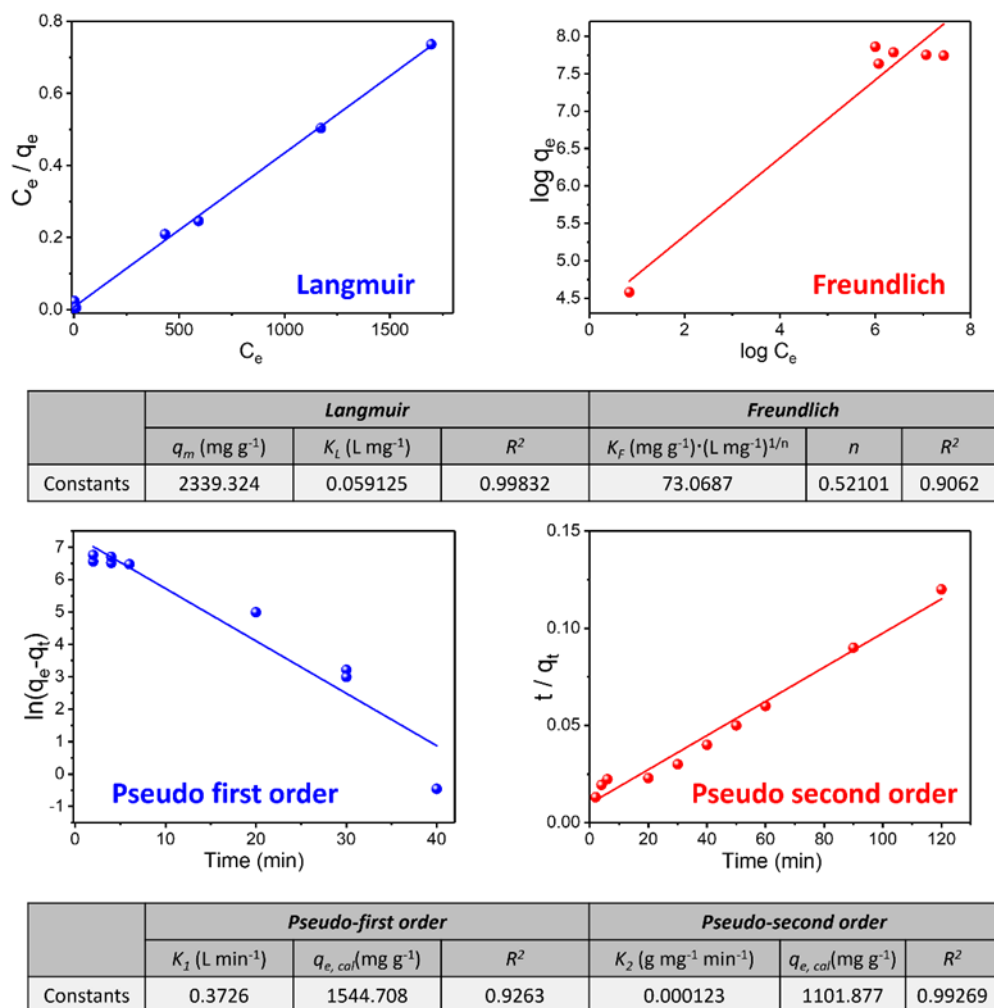
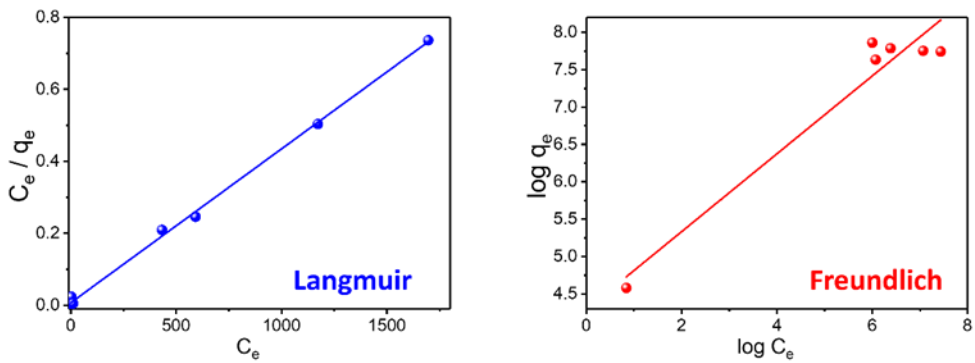
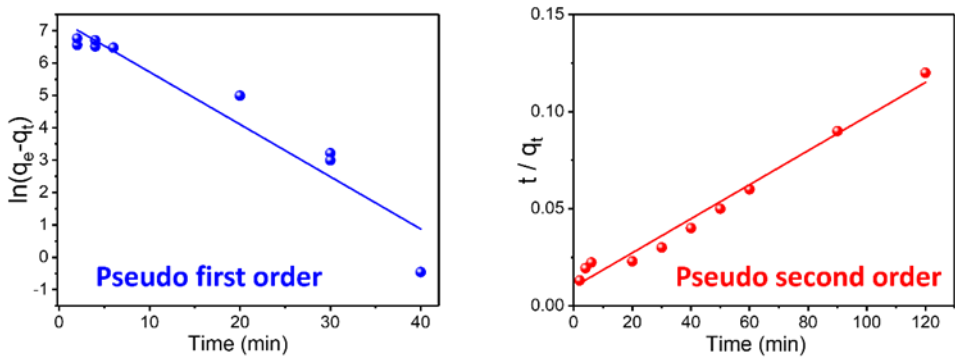


Figure 2.5. Absorption kinetics and isotherms of whitlockite (WH) for Pb²⁺ absorption. The Langmuir and Freundlich models were applied to investigate the absorption capacity, while the pseudo-first and pseudo-second order models were used to describe the absorption kinetics. Maximum amount of Pb²⁺ ions required to form a monolayer (q_m), Langmuir constant (K_L), Freundlich constant or an approximate indicator of the absorption capacity (K_F), the amount of absorbed Pb²⁺ at equilibrium (q_e), the constant of pseudo-first order (k_1) and the constant of pseudo-second order (k_2)



	Langmuir			Freundlich		
	q_m (mg g ⁻¹)	K_L (L mg ⁻¹)	R^2	K_f (mg g ⁻¹)·(L mg ⁻¹) ^{1/n}	n	R^2
Constants	2339.324	0.059125	0.99832	73.0687	0.52101	0.9062



	Pseudo-first order			Pseudo-second order		
	K_1 (L min ⁻¹)	$q_{e,cal}$ (mg g ⁻¹)	R^2	K_2 (g mg ⁻¹ min ⁻¹)	$q_{e,cal}$ (mg g ⁻¹)	R^2
Constants	0.3726	1544.708	0.9263	0.000123	1101.877	0.99269

Figure 2.6. Adsorption kinetics and isotherms of hydroxyapatite (HAP) for Pb²⁺ absorption. The Langmuir and Freundlich models were applied to investigate the absorption capacity, while the pseudo-first and pseudo-second order models were used to describe the absorption kinetics.

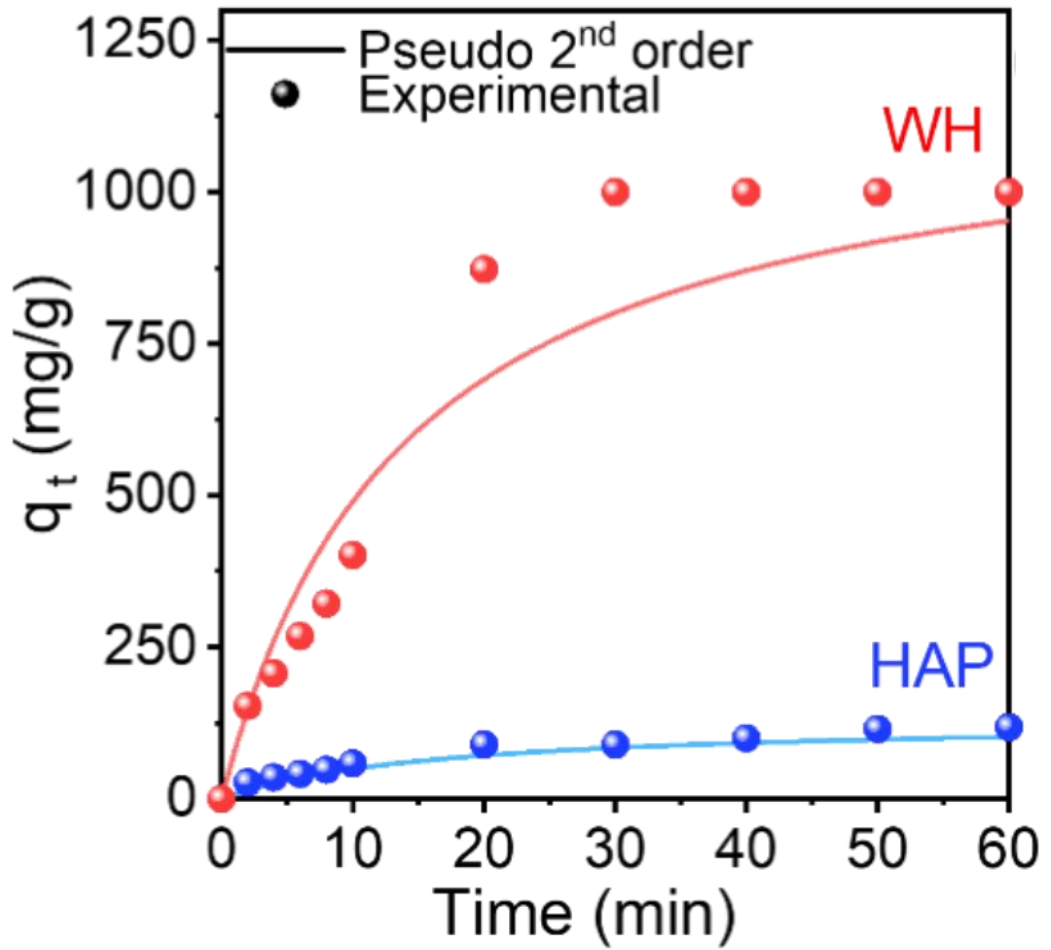


Figure 1.7 Pseudo-second order kinetics plot of Pb²⁺ absorption on HAP and WH.

In addition, Figure 2.8 demonstrates that the Pb^{2+} removal process can be represented by the Langmuir model: as a result, WH exhibits a much higher absorption capacity (2339 mg g^{-1}) than HAP (239 mg g^{-1}).

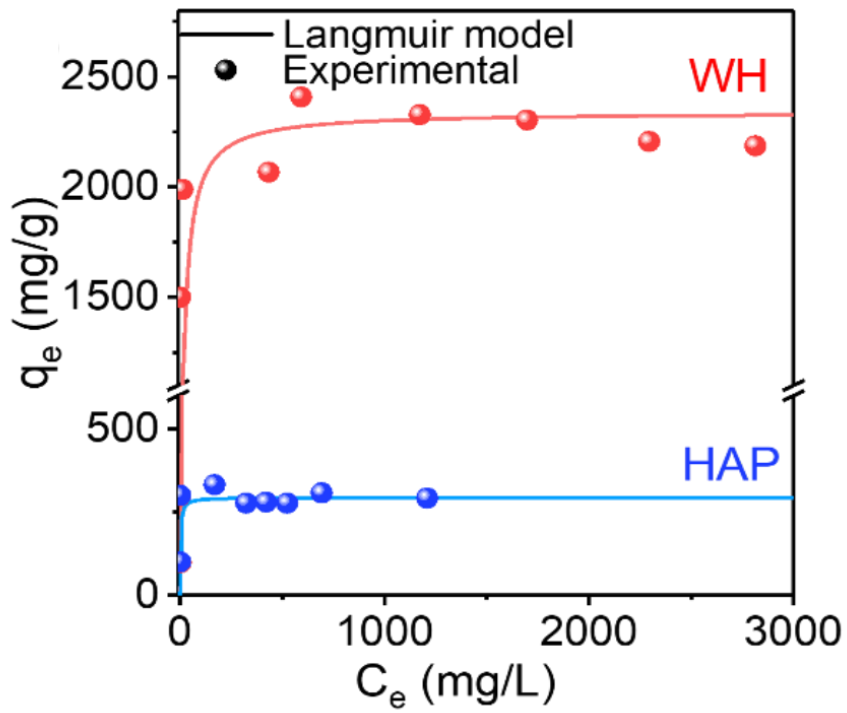


Figure 2.8 Langmuir sorption isotherm of Pb²⁺ by HAP and WH

Figure 2.9 presents the Pb absorption capacities of various absorbents obtained in previous studies.[16,17,19,21,29–44] Biomineral HAP is known as one of the most promising candidates as an absorbent for Pb²⁺ removal. Interestingly, WH exhibited the highest absorption capacity, which was 1.68 times higher than the highest recorded value for HAP (1269.01 mg g⁻¹).[17] Brunauer-Emmett-Teller (BET) surface areas and Zeta potentials were also measured to investigate the surface properties of HAP and WH. WH exhibits a smaller BET surface (43.2 m² g⁻¹) than HAP (77.8 m² g⁻¹).

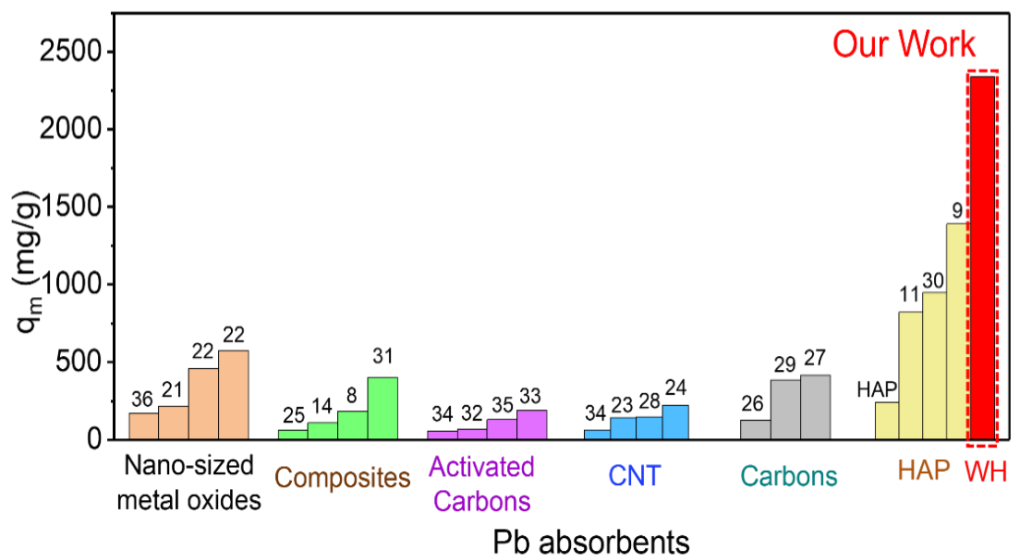


Figure 3.9 Langmuir sorption isotherm of Pb^{2+} by HAP and WH

In addition, it should be noted that the isoelectric point of WH was higher than that of HAP, as shown in Figure 2.10. The smaller BET surface area and more positive surface charge of WH may constitute a drawback in the absorption of positive Pb^{2+} ions in comparison to HAP.

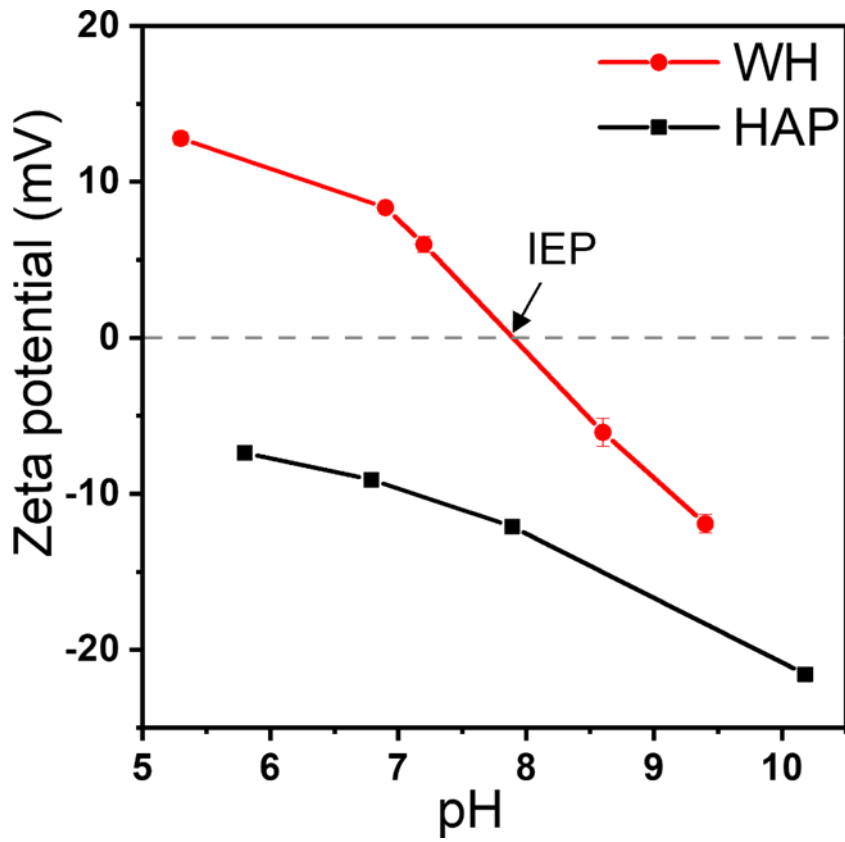


Figure 2.10 Zeta potential of hydroxyapatite (HAP) and whitlockite (WH). WH showed a higher positive Zeta potential and isoelectric point (IEP) in the given pH region.

2.3.3 characterization of Pb absorbed WH and HAP

To understand the exceptionally high absorption capacity of WH NPs, we observed their phase transformation after Pb^{2+} absorption (Pb-WH) at various Pb^{2+} concentrations in the range 0–3000 ppm, as shown in Figure 2.11 and Figure 2.12

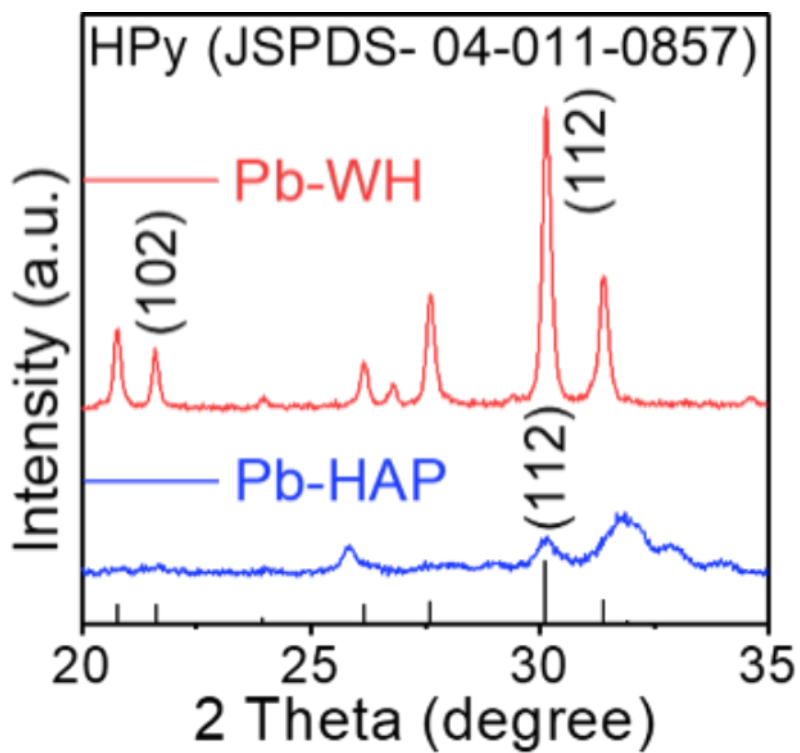


Figure 2.11 XRD patterns of whitlockite (WH) and hydroxyapatite (HAP) nanoparticles after Pb^{2+} absorption.

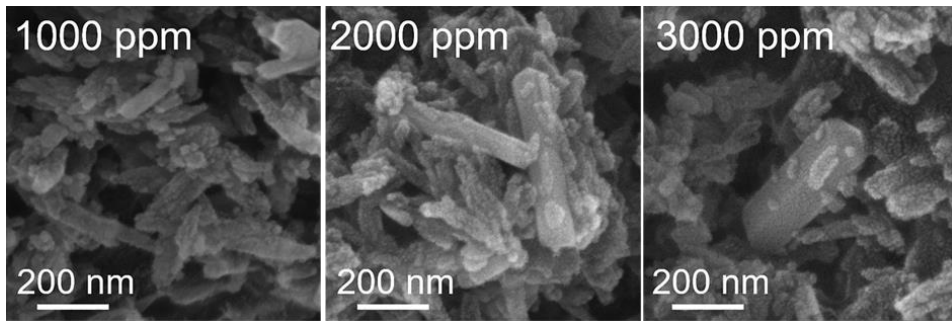


Figure 2.12 Field-emission scanning electron microscopy images of hydroxyapatite at various Pb^{2+} concentrations (1000–3000 ppm).

The XRD patterns of HAP NPs after Pb^{2+} absorption (Pb-HAP) exhibited two complex phases: HAP and hydroxypyromorphite (HPy, $\text{Pb}_{10}(\text{PO}_4)_6(\text{OH})_2$), whose peak positions and intensities did not vary for Pb^{2+} concentrations higher than 1000 ppm. In contrast, WH NPs transformed completely into HPy already at 1000 ppm Pb^{2+} . In addition, the intensity of the main diffraction peaks of HPy at $2\theta = 30.14^\circ$, corresponding to the (112) plane, increased gradually with an increase in Pb^{2+} concentration, as shown in Figure 2.13. Furthermore, we analyzed the HPy/absorbents ratio after Pb^{2+} absorption as a function of Pb^{2+} concentration using the Rietveld method, as shown in Figure 2.14. The HPy/Pb-HAP ratio increased to 16.78% at 1000 ppm Pb^{2+} and did not change significantly at higher Pb^{2+} concentrations. In contrast, the HPy/Pb-WH ratio was equal to 42.7%, 85.5%, and 100% for 1000, 2000, and 3000 ppm, respectively, which is consistent with its absorption capacity. In addition, the 50 nm-sized rhombohedral WH NPs readily transformed into nanowires with lengths of several micrometers ($1.6 \pm 0.56 \mu\text{m}$) after Pb^{2+} absorption, as shown in the inset of Figure 2.14. This dramatic change in morphology might have been induced by a dissolution and recrystallization mechanism characterizing the phase transformation of WH into HPy, rather than by ion exchange.

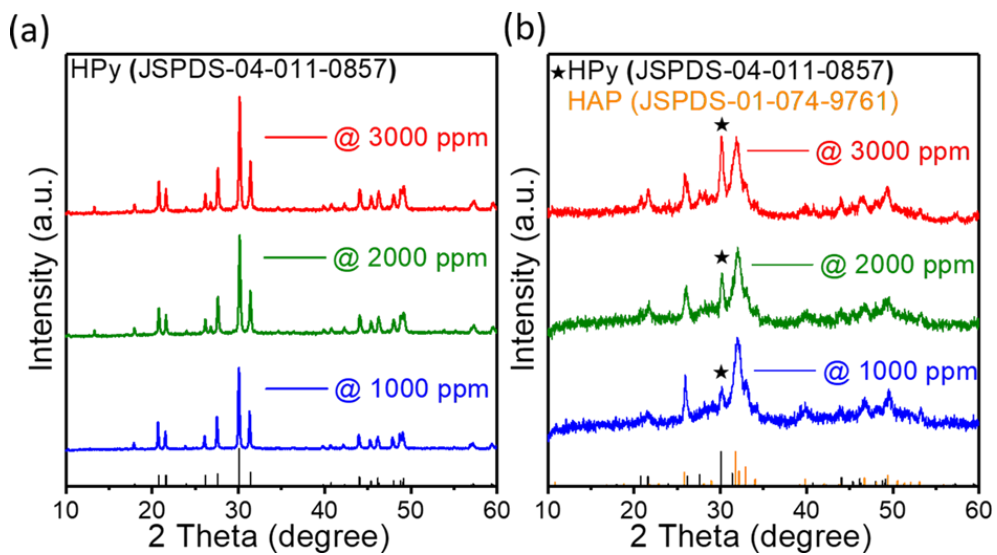


Figure 2.13 Field-emission scanning electron microscopy images of hydroxyapatite at various Pb^{2+} concentrations (1000–3000 ppm).

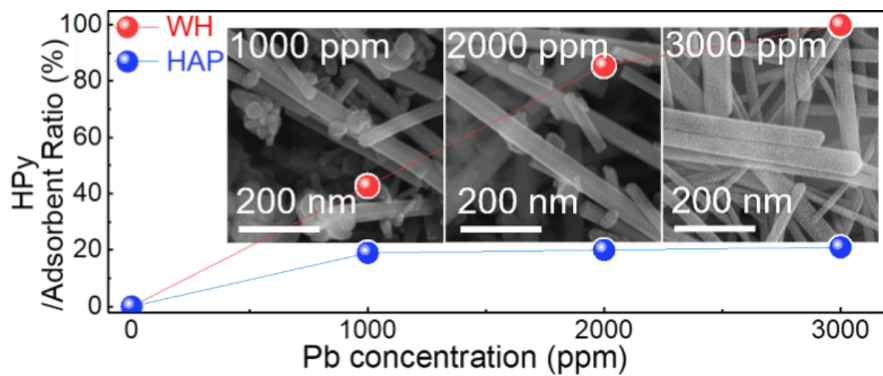
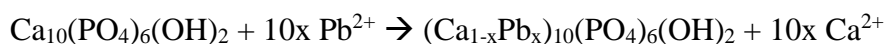


Figure 2.14 Calculated hydroxypyromorphite (HPy) ratio after Pb^{2+} absorption via the Rietveld method (inset shows a field-emission scanning electron microscopy image of Pb-WH at the initial Pb^{2+} concentration).

2.3.4 Pb absorption mechanism of HAP

The mechanism of Pb^{2+} absorption on HAP NPs is well known: it is characterized by the ionic exchange of Pb^{2+} cations diffusing into the HAP structure and substituting Ca^{2+} cations primarily at the Ca(2) sites.[45–49] The positively charged Pb^{2+} ions react with the negatively charged surface of HAP NPs, subsequently forming a $(\text{Pb}_x\text{Ca}_{1-x})_{10}(\text{PO}_4)_6(\text{OH})_2$ layer on the surface of HAP NPs, as illustrated in Figure 2.15.[50] Figure 2.16(a) shows the transmission electron microscopy (TEM) images of HAP NPs after Pb^{2+} absorption for 2 h. We observed two simultaneous morphologies: the expanded initial one and a hexagonal prism morphology. The ionic radius of the Pb^{2+} ion (1.2 Å) is higher than that of Ca^{2+} (0.99 Å), which determines an increase in volume during the phase transformation from HAP to HPy according to the following chemical reaction:



In addition, the morphology of the apatite structure depends on the Pb^{2+} content in $(\text{Pb}_x\text{Ca}_{1-x})_{10}(\text{PO}_4)_6(\text{OH})_2$. [50] For $x < 0.8$, the original particle size increased from 123.87 ± 29.38 nm to 197.76 ± 46.57 nm, while for $x > 0.8$, $(\text{Ca}_{1-x}\text{Pb}_x)_{10}(\text{PO}_4)_6(\text{OH})_2$ assumed the hexagonal prism morphology with further elongation to 246.75 ± 15.15 nm. Figure 2.16 (b) and Table 1 show the energy dispersive spectroscopy (EDS) elemental maps corresponding to the TEM images. The content of Ca^{2+} ions remained

3.62 % in $(\text{Ca}_{1-x}\text{Pb}_x)_{10}(\text{PO}_4)_6(\text{OH})_2$, indicating some limitations of HAP as a Pb^{2+} absorbent. The reason for this phenomenon lies in the passivation effect of Pb^{2+} on the HAP surface, which slows the ion exchange by Pb^{2+} diffusion and blocks the protonation of PO_4^{3-} sites in HAP, resulting in a lower absorption capacity than that of WH NPs, as shown in Figure 2.4. [45,51,52]

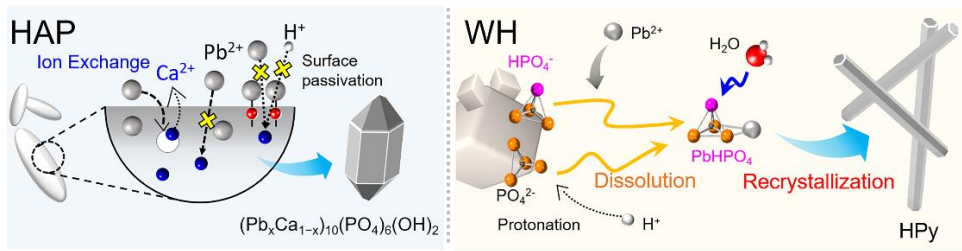


Figure 2.15 Schematic illustration of Pb^{2+} absorption mechanisms: ion exchange in HAP and dissolution followed by recrystallization in WH

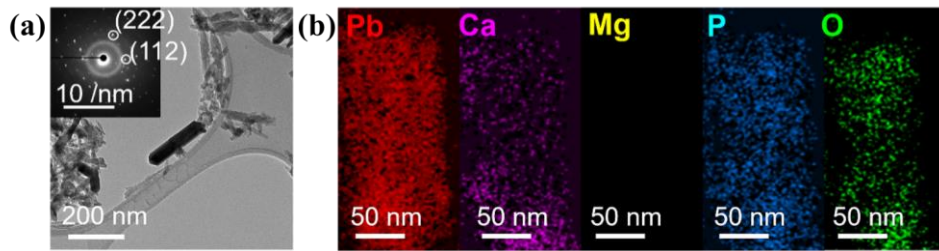


Figure 2.16 Schematic illustration of Pb^{2+} absorption mechanisms: ion exchange in HAP and dissolution followed by recrystallization in WH

Table 1. Energy dispersive X-ray spectroscopy analysis of Pb-absorbed whitlockite (Pb-WH) and hydroxyapatite (Pb-HAP). Pb-WH transformed into pure HPy in the absence of Ca^{2+} or Mg^{2+} residues, while some Ca^{2+} remained in Pb-HAP, resulting in a $(\text{Pb}_x\text{Ca}_{1-x})_{10}(\text{PO}_4)_6(\text{OH})_2$ solid solution.

Element	Pb-WH [at%]	Pb-HAP [at%]
O	66.78	64.3
P	9.12	9.61
Mg	0.00	0.00
Ca	0.00	3.62
Pb	24.09	22.47
Total	100.00	100.00

To confirm the effect of crystallinity on the Pb absorption performance, HAP was annealed at 400°C for 6hr. The XRD patterns in Figure 17 show crystallinity development without any impurities in HAP after annealing process. The high crystalline HAP NP removed Pb ions more efficiently than low crystalline HAP NP as shown in Figure 18.

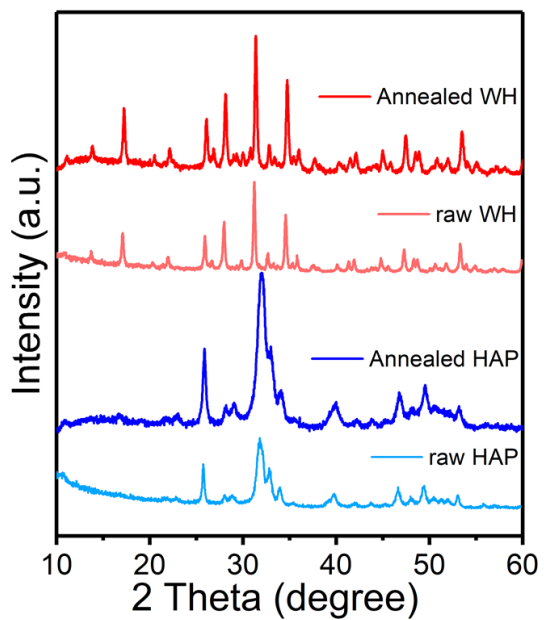


Figure 2.17 XRD patterns of raw and absorbents (a) raw WH, (b) annealed WH, (c) raw HAP and (d) annealed HAP.

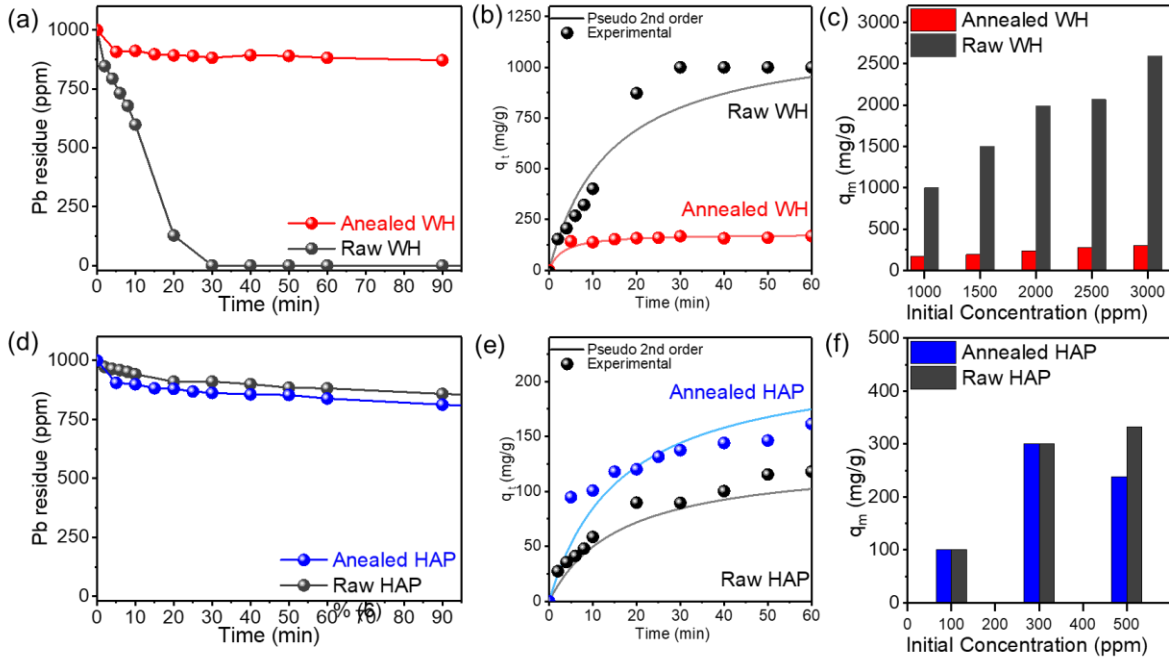


Figure 2.18 Pb²⁺ absorption behavior of by annealed WH and raw WH. (a) Pb²⁺ absorption, (b) Pseudo-second order kinetics plot of Pb²⁺ absorption and (c) Pb²⁺ absorption capacity according to initial Pb concentration. Pb²⁺ absorption behavior of by annealed HAP and raw HAP. (a) Pb²⁺ absorption, (b) Pseudo-second order kinetics plot of Pb²⁺ absorption and (c) Pb²⁺ absorption capacity according to initial Pb concentration.

2.3.5 Pb absorption mechanism of WH

Figure 19 (a) and (b) show the TEM images and corresponding EDS elemental mapping of WH NPs after the reaction with Pb^{2+} . The obtained HPy exhibits a nanowire shape with a particle length of 1.09 μm and growth along the [210] direction within a single-crystalline phase. In addition, no residual metal ions, i.e., Ca^{2+} and Mg^{2+} , were observed in the HPy phase, as shown in Figure 19 (b) and Table 1.

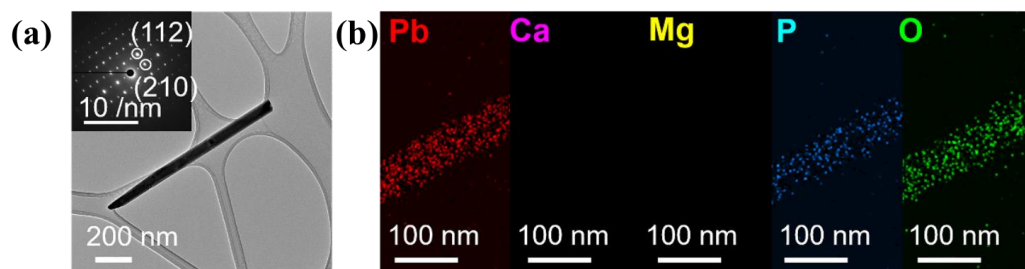
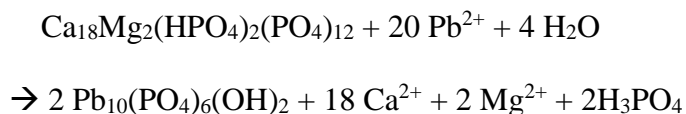


Figure 2.19 (a)HR-TEM image and SAED pattern (inset) of Pb-WH: the d-spacing value in the SAED pattern is in good agreements with the crystal structure data of HPy (JCPDS 04-011-0857). (b) EDS results for Pb-WH proving the absence of Ca^{2+} and Mg^{2+} cations.

The Pb²⁺ absorption mechanism of WH likely proceeds through H⁺ ion-catalyzed dissolution and recrystallization in a Pb²⁺-containing aqueous solution. WH can easily react with Pb²⁺ ions owing to their strong interaction with HPO₄²⁻ groups, followed by the inner PO₄³⁻ ions. In this way, the WH structure is continuously protonated in an aqueous solution, inducing the dissolution and recrystallization process that can be exploited for Pb²⁺ removal, as illustrated in Figure 2.15.[51,53] The chemical reaction illustrating the absorption of Pb²⁺ to WH is the following:



The XRD patterns of annealed WH in Figure 2.17 show crystallinity development without any heterophase. As shown in Figure 2.18, Pb absorption performance of WH dramatically decreased after annealing process. The high crystalline WH NP can retard the dissolution and reprecipitation mechanism for removal Pb ions because of more stable surface than low crystalline WH NP, as shown in Figure 2.18.

2.3.6 Reutilization of Pb

Following the above results, we postulated that a single-crystalline phase of HPy obtained from WH NPs could provide high-purity PbI_2 powder via a precipitation method, and that this could be employed in the recycling of PSCs using an I^- aqueous solution.[6,54] Figure 2.20 shows the field-emission scanning electron microscopy (FE-SEM) images of PbI_2 obtained from HAP and WH NPs.

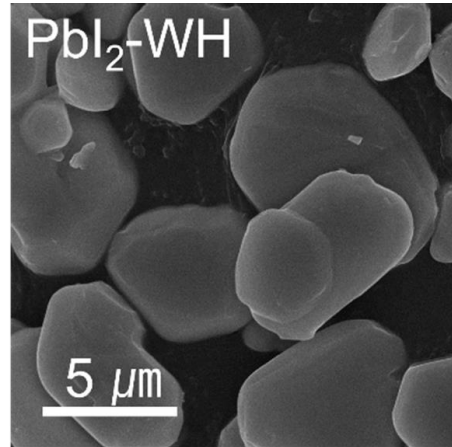
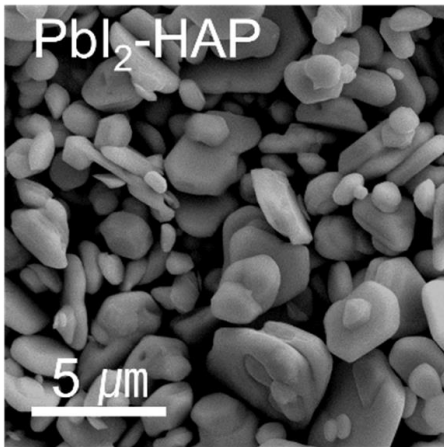


Figure 2.20 Field-emission scanning electron microscopy images of as-obtained PbI₂-hydroxyapatite (PbI₂-HAP) and PbI₂-whitlockite (PbI₂-WH).

The PbI_2 powder recycled from WH NPs (PbI_2 -WH) contained particles approximately three times larger than HAP NPs ($2.58 \pm 0.67 \mu\text{m}$). In addition, PbI_2 -WH showed high crystallinity by exhibiting more intense XRD peaks than PbI_2 -HAP (Figure 2.21). The full-width half maximum (FWHM) for the (001) peak of XRD patterns for PbI_2 -W and PbI_2 -H are 0.08419 and 0.09343, respectively. The higher purity and crystallinity of PbI_2 -W enhance the performance of PSC by reducing defects in perovskite.[55]

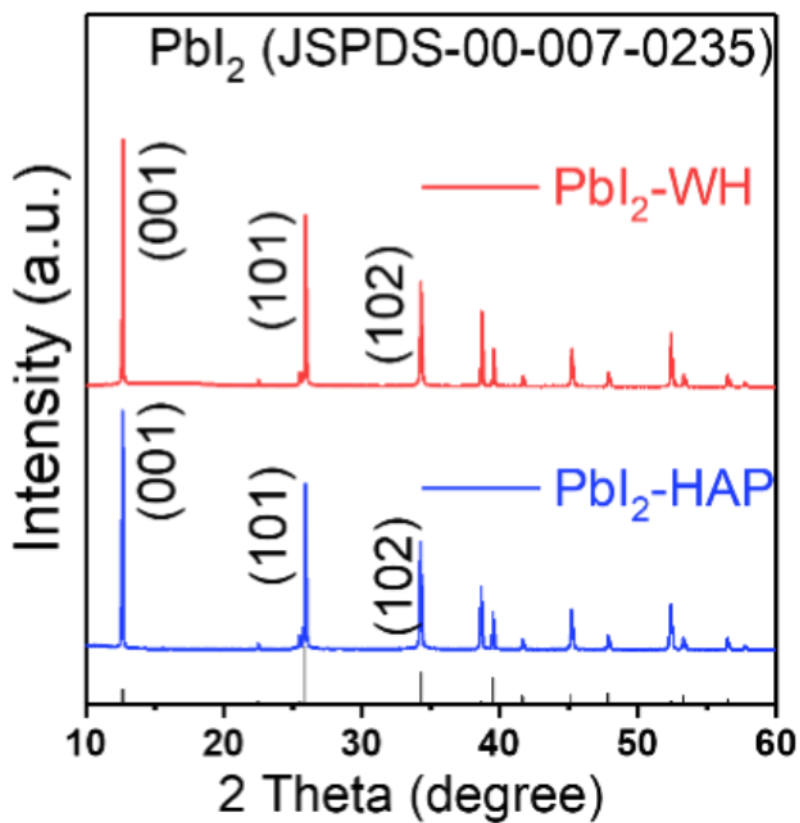


Figure 2.21 XRD patterns of PbI_2 -HAP and PbI_2 -WH are in good agreement with the crystal structure data of PbI_2 (JCPDS 00-007-0235).

To assess the effect of PbI₂ purity and crystallinity on its performance in PSCs, we fabricated PSCs using recycled PbI₂-HAP and PbI₂-WH as well as commercial PbI₂ (PbI₂-C, 99.99% purity) as precursors. The detailed characteristics of PbI₂-C, PbI₂-WH and PbI₂-HAP are shown in Figure 2.22 and 2.23. Perovskite film based on PbI₂-C and PbI₂-WH exhibits higher crystallinity and coverage than film based on PbI₂-HAP, as illustrated in Figure 2.24. Figure 2.25 shows the steady-state photoluminescence (PL) of perovskite films containing PbI₂-HAP, PbI₂-WH, and PbI₂-C. Interestingly, the PbI₂-WH and PbI₂-C films exhibited stronger PL intensities than PbI₂-HAP. In addition, space charge limited current measurements were used to calculate the defect densities, as shown in Figure 26. The trap filled limit voltage of perovskite films was 0.340 V for PbI₂-HAP, 0.260 V for PbI₂-WH, and 0.243 V for PbI₂-C. The trap densities of PbI₂-WH- and PbI₂-C-based films were similar, with respective values of 8.218×10^{15} and $7.681 \times 10^{15} \text{ cm}^{-3}$, and lower than the value of $10.72 \times 10^{15} \text{ cm}^{-3}$ of PbI₂-HAP. The performances of PSCs are presented in Table 2. This result indicates that the high purity of PbI₂ affects the defect formation and coverage on the perovskite films during the crystallization process, shown in Figure 2.24. Finally, PbI₂-WH-based PSCs achieved an average PCE of $19.00 \pm 1.40\%$, which was remarkably similar to that of PbI₂-C based cells (Figure 2.27 and Figure 2.28).

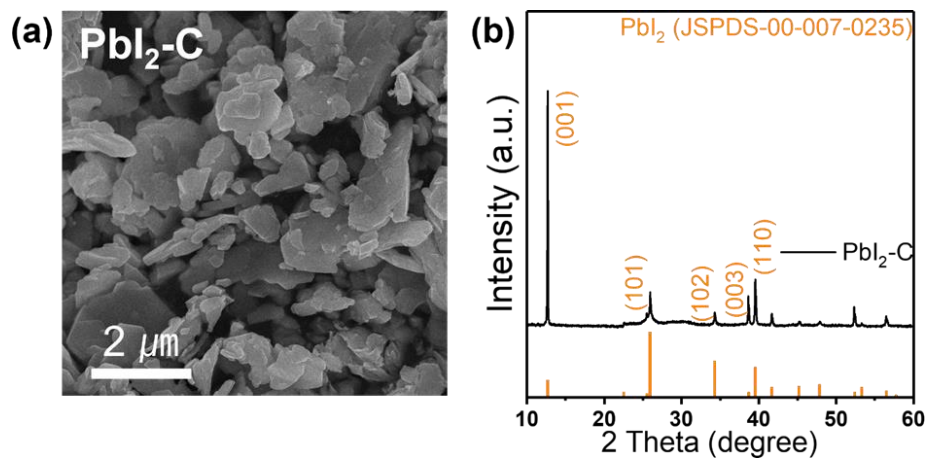


Figure 2.22 Field-emission scanning electron microscopy image (a) and X-ray diffraction pattern (b) of commercial PbI_2 ($\text{PbI}_2\text{-C}$).

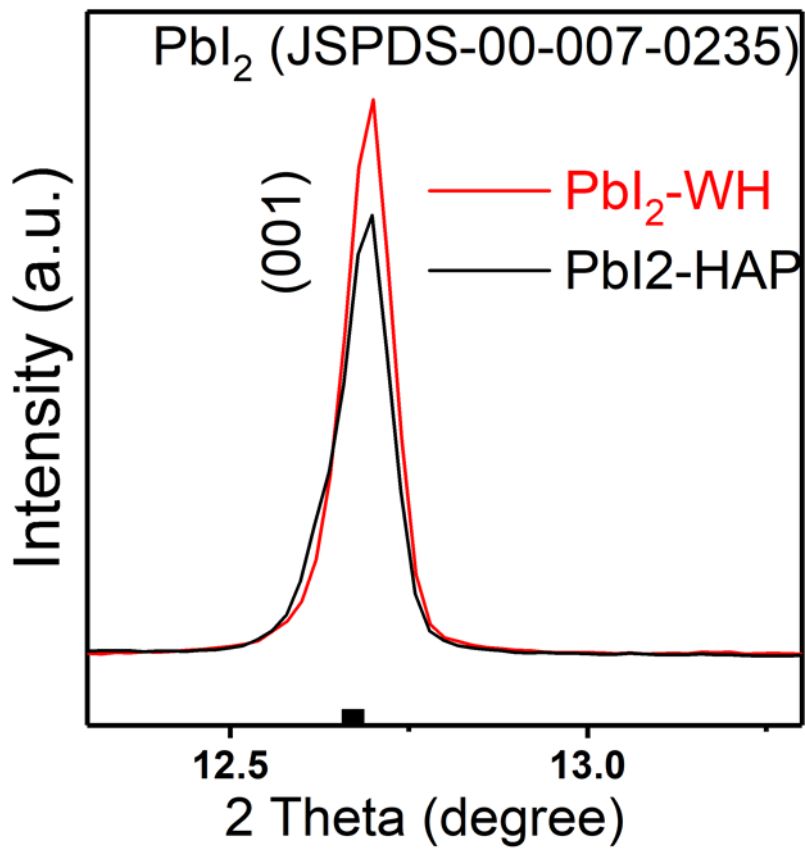


Figure 2.23 Detailed comparison of peak intensity between PbI₂-WH and PbI₂-HAP

Table 2. Characterization of the performances of commercial PbI₂ (PbI₂-C), PbI₂-hydroxyapatite (PbI₂-HAP), and PbI₂-whitlockite (PbI₂-WH) in PSCs. Short-circuit current density (J_{sc}), open-circuit voltage (V_{oc}), power conversion efficiency (PCE) and fill factor (FF).

	J _{sc} [mA cm ⁻²]	V _{oc} [V]	PCE [%]	FF
PbI ₂ – C	21.72 ± 0.36	1.14 ± 0.01	19.31 ± 0.94	0.78 ± 0.04
PbI ₂ – WH	21.70 ± 0.37	1.14 ± 0.02	19.00 ± 1.40	0.77 ± 0.05
PbI ₂ – HAP	21.47 ± 0.28	1.09 ± 0.02	16.85 ± 1.54	0.72 ± 0.05

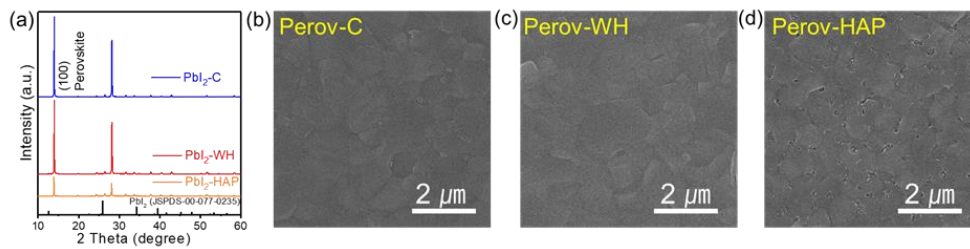


Figure 24. Properties of perovskite films. (a) XRD patterns of perovskite film based on (b) PbI₂-C, (c) PbI₂-WH and (d) PbI₂-HAP.

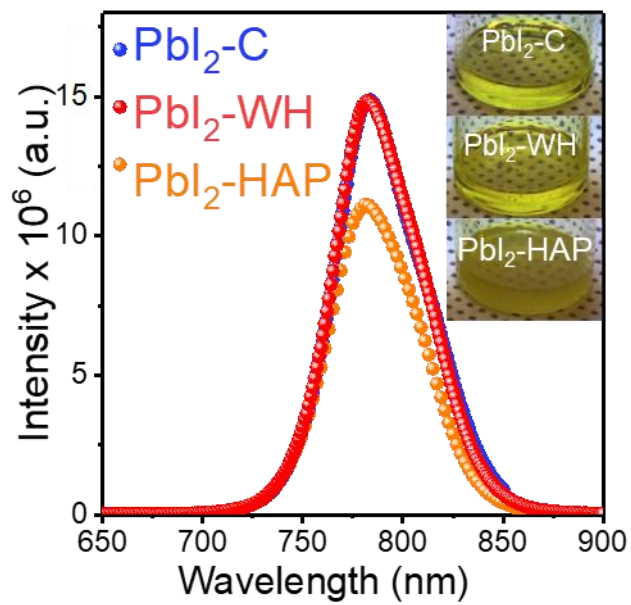


Figure 25. Steady-state photoluminescence with PbI₂-HAP, PbI₂-WH, and commercial PbI₂ (PbI₂-C).

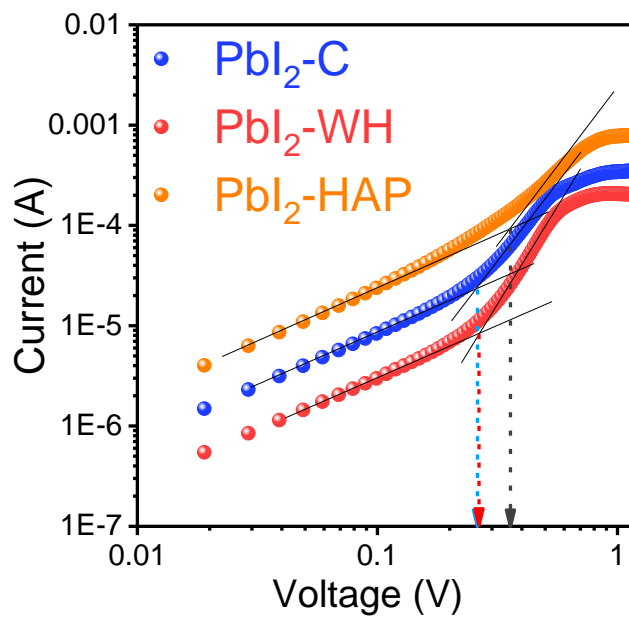


Figure 26. space charge limited current measurements (glass/ITO/SnO₂/perovskite/PCBM/Au) with PbI₂-HAP, PbI₂-WH, and commercial PbI₂ (PbI₂-C).

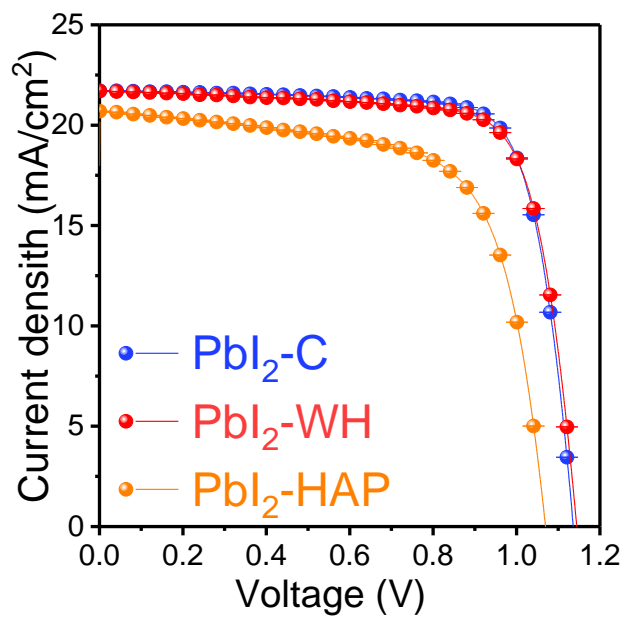


Figure 2.27 the best PCE of perovskite films (glass/ITO/SnO₂/perovskite/spiro-OMeTAD/Au) with PbI₂-HAP, PbI₂-WH, and commercial PbI₂ (PbI₂-C).

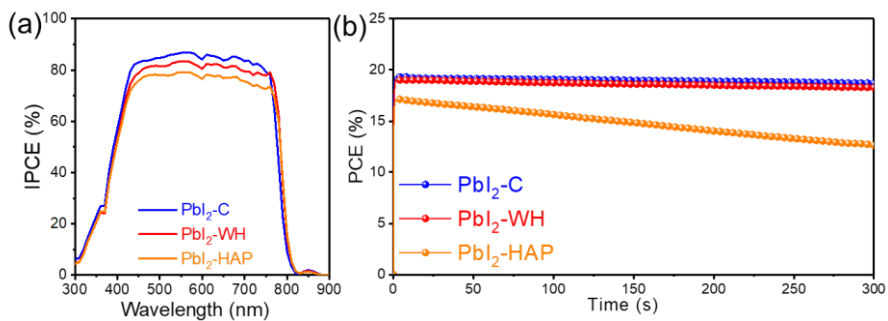


Figure 2.28 Performance of PSC fabricated with PbI₂-C, PbI₂-WH and PbI₂-HAP. (a) External quantum efficiency and (b) steady state power conversion efficiency.

2.4 Concluding Remarks

We investigated novel biomimetic WH NPs as a Pb^{2+} absorbent synthesized via simple wet precipitation and applied in a high-throughput Pb^{2+} recycling process. The synthesized WH NPs presented a rhombohedral structure with an average size of 50 nm and XRD patterns of synthesized WH is in good agreement with the crystal structure data. Interestingly, the Pb^{2+} removal properties of WH NPs were associated with a surprising absorption capacity of 2339 mg g^{-1} compared to 239 mg g^{-1} for the more common HAP NPs, thereby exhibiting the highest value ever recorded among Pb-absorbing materials. The reason for such different absorption capacities lies in the different mechanisms taking place in HAP and WH in contact with the Pb-containing solution. The HAP capacity toward Pb^{2+} absorption is limited by the formation of a passivated Pb^{2+} surface layer, which suppresses ion exchange with dissolved Pb^{2+} and the protonation of PO_4^{3-} groups in HAP. In contrast, WH is readily dissolved owing to its strong interaction with Pb^{2+} ions and rapid protonation in an aqueous solution, which induce the recrystallization into HPy in a highly crystalline form. The highly crystalline HPy was recycled to high-purity PbI_2 , which provided a similar photovoltaic performance in PSCs compared to that of commercial PbI_2 and equal to 19.00% PCE. In conclusion, owing to their excellent Pb^{2+} absorption capacity and the possibility of recycling PbI_2 , WH

NPs are the most promising absorbent material for high-throughput and eco-friendly PSCs recycling.

References

- [1] S.M. Kim, P.M. Abdala, M. Broda, D. Hosseini, C.C. Copéret, C. Mü, Integrated CO₂ Capture and Conversion as an Efficient Process for Fuels from Greenhouse Gases, (2018). <https://doi.org/10.1021/acscatal.7b03063>.
- [2] Y. Duan, D.C. Sorescu, ARTICLES YOU MAY BE INTERESTED IN A climbing image nudged elastic band method for finding saddle points and minimum energy paths The CO₂ capture properties of alkaline earth metal oxides and hydroxides: A combined density functional theory and lattice phonon dynamics study, *J. Chem. Phys.* 133 (2010) 9901. <https://doi.org/10.1063/1.3473043>.
- [3] U. Stoin, Z. Barnea, Y. Sasson, New technology for post-combustion abatement of carbon dioxide via an in situ generated superoxide anion-radical, *RSC Adv.* 4 (2014) 36544–36552. <https://doi.org/10.1039/C4RA03844D>.
- [4] U. Stoin, A.I. Shames, Y. Sasson, Novel technology for the rapid total mineralization of carbon tetrachloride under ambient conditions †, (n.d.). <https://doi.org/10.1039/c3ra44204g>.
- [5] I.R. Gibson, W. Bonfield, Novel synthesis and characterization of an AB-type carbonate-substituted hydroxyapatite, (2001). <https://doi.org/10.1002/jbm.10044>.
- [6] S.Y. Park, J.S. Park, B.J. Kim, H. Lee, A. Walsh, K. Zhu, D.H. Kim, H.S. Jung, Sustainable lead management in halide perovskite solar cells, *Nat. Sustain.* 3 (2020) 1044–1051. <https://doi.org/10.1038/s41893-020-0586-6>.
- [7] Z. Li, X. Wu, B. Li, S. Zhang, D. Gao, Y. Liu, X. Li, N. Zhang, X. Hu, C. Zhi, A. K-Y Jen, Z. Zhu, Z. Li, X. Wu, B. Li, S. Zhang, D. Gao, Y. Liu, X. Li, A. K-Y Jen, Z. Zhu, N. Zhang, C. Zhi, X. Hu, Sulfonated Graphene Aerogels Enable Safe-to-Use Flexible Perovskite Solar Modules, *Adv. Energy Mater.* (2021) 2103236. <https://doi.org/10.1002/AENM.202103236>.
- [8] S. Wu, Z. Li, M.Q. Li, Y. Diao, F. Lin, T. Liu, J. Zhang, P. Tieu, W. Gao, F. Qi, X. Pan, Z. Xu, Z. Zhu, A.K.Y. Jen, 2D metal–organic framework for stable perovskite solar cells with minimized lead leakage, *Nat. Nanotechnol.* 15 (2020) 934–940. <https://doi.org/10.1038/s41565-020-0765-7>.
- [9] Z. Li, X. Wu, S. Wu, D. Gao, H. Dong, F. Huang, X. Hu, A.K.Y. Jen, Z.

- Zhu, An effective and economical encapsulation method for trapping lead leakage in rigid and flexible perovskite photovoltaics, *Nano Energy*. 93 (2022) 10685. <https://doi.org/10.1016/j.nanoen.2021.106853>.
- [10] G. Bin Xiao, L.Y. Wang, X.J. Mu, X.X. Zou, Y.Y. Wu, J. Cao, Lead and Iodide Fixation by Thiol Copper(II) Porphyrin for Stable and Environmental-Friendly Perovskite Solar Cells, *CCS Chem*. 3 (2021) 25–36. <https://doi.org/10.31635/CCSCHEM.021.202000516>.
- [11] Y. Liang, P. Song, H. Tian, C. Tian, W. Tian, Z. Nan, Y. Cai, P. Yang, C. Sun, J. Chen, L. Xie, Q. Zhang, Z. Wei, Lead Leakage Preventable Fullerene-Porphyrin Dyad for Efficient and Stable Perovskite Solar Cells, *Adv. Funct. Mater.* n/a (2021) 2110139. <https://doi.org/https://doi.org/10.1002/adfm.202110139>.
- [12] W. Chen, Z. Lu, B. Xiao, P. Gu, W. Yao, J. Xing, A.M. Asiri, K.A. Alamry, X. Wang, S. Wang, Enhanced removal of lead ions from aqueous solution by iron oxide nanomaterials with cobalt and nickel doping, *J. Clean. Prod.* 211 (2019) 1250–1258. <https://doi.org/10.1016/J.JCLEPRO.2018.11.254>.
- [13] J. Al Abdullah, A.G. Al Lafi, W. Al Masri, Y. Amin, T. Alnana, Adsorption of Cesium, Cobalt, and Lead onto a Synthetic Nano Manganese Oxide: Behavior and Mechanism, *Water. Air. Soil Pollut.* 227 (2016). <https://doi.org/10.1007/s11270-016-2938-4>.
- [14] Y. Tan, M. Chen, Y. Hao, High efficient removal of Pb (II) by amino-functionalized Fe₃O₄ magnetic nano-particles, *Chem. Eng. J.* 191 (2012) 104–111. <https://doi.org/10.1016/j.cej.2012.02.075>.
- [15] E.N. Zare, M.M. Lakouraj, N. Kasirian, Development of effective nanobiosorbent based on poly m-phenylenediamine grafted dextrin for removal of Pb (II) and methylene blue from water, *Carbohydr. Polym.* 201 (2018) 539–548. <https://doi.org/10.1016/j.carbpol.2018.08.091>.
- [16] Y.X. Ma, Y.L. Kou, D. Xing, P.S. Jin, W.J. Shao, X. Li, X.Y. Du, P.Q. La, Synthesis of magnetic graphene oxide grafted polymaleicamide dendrimer nanohybrids for adsorption of Pb(II) in aqueous solution, *J. Hazard. Mater.* 340 (2017) 407–416. <https://doi.org/10.1016/J.JHAZMAT.2017.07.026>.
- [17] Y.-G. Bi, D. Liu, X.-M. Liu, S.-Q. Zhou, Preparation and characterization of nano-hydroxyapatite and its adsorption behavior toward copper ions,

- Nanosci. Nanotechnol. Lett. 9 (2017) 810–816.
- [18] L. Hao, Y. Lv, H. Song, The morphological evolution of hydroxyapatite on high-efficiency Pb2 + removal and antibacterial activity, *Microchem. J.* 135 (2017) 16–25. <https://doi.org/10.1016/j.microc.2017.07.008>.
- [19] X. Zou, Y. Zhao, Z. Zhang, Preparation of hydroxyapatite nanostructures with different morphologies and adsorption behavior on seven heavy metals ions, *J. Contam. Hydrol.* 226 (2019) 103538. <https://doi.org/10.1016/j.jconhyd.2019.103538>.
- [20] B.J. Kim, D.H. Kim, S.L. Kwon, S.Y. Park, Z. Li, K. Zhu, H.S. Jung, Selective dissolution of halide perovskites as a step towards recycling solar cells, *Nat. Commun.* 7 (2016). <https://doi.org/10.1038/ncomms11735>.
- [21] Z. Zhang, X. Wang, H. Wang, J. Zhao, Removal of Pb(II) from aqueous solution using hydroxyapatite/calcium silicate hydrate (HAP/C-S-H) composite adsorbent prepared by a phosphate recovery process, *Chem. Eng. J.* 344 (2018) 53–61. <https://doi.org/10.1016/j.cej.2018.03.066>.
- [22] G. Graziani, M. Boi, M. Bianchi, A review on ionic substitutions in hydroxyapatite thin films: Towards complete biomimetism, *Coatings.* 8 (2018). <https://doi.org/10.3390/COATINGS8080269>.
- [23] C. Chen, Y. Xu, S. Wu, S. Zhang, Z. Yang, W. Zhang, H. Zhu, Z. Xiong, W. Chen, W. Chen, CaI2: a more effective passivator of perovskite films than PbI2 for high efficiency and long-term stability of perovskite solar cells, *J. Mater. Chem. A.* 6 (2018) 7903–7912. <https://doi.org/10.1039/C7TA11280G>.
- [24] C. Lu, J. Zhang, D. Hou, X. Gan, H. Sun, Z. Zeng, R. Chen, H. Tian, Q. Xiong, Y. Zhang, Y. Li, Y. Zhu, Calcium doped MAPbI₃ with better energy state alignment in perovskite solar cells, *Appl. Phys. Lett.* 112 (2018) 193901. <https://doi.org/10.1063/1.5020840>.
- [25] H.L. Jang, K. Jin, J. Lee, Y. Kim, S.H. Nahm, K.S. Hong, K.T. Nam, Revisiting whitlockite, the second most abundant biomineral in bone: Nanocrystal synthesis in physiologically relevant conditions and biocompatibility evaluation, *ACS Nano.* 8 (2014) 634–641. <https://doi.org/10.1021/nn405246h>.
- [26] H.L. Jang, H.K. Lee, K. Jin, H.Y. Ahn, H.E. Lee, K.T. Nam, Phase

- transformation from hydroxyapatite to the secondary bone mineral, whitlockite, *J. Mater. Chem. B.* 3 (2015) 1342–1349.
<https://doi.org/10.1039/c4tb01793e>.
- [27] X. Zhou, J. Nie, B. Du, 4-(2-Pyridylazo)-resorcinol Functionalized Thermosensitive Ionic Microgels for Optical Detection of Heavy Metal Ions at Nanomolar Level, *ACS Appl. Mater. Interfaces.* 7 (2015) 21966–21974.
<https://doi.org/10.1021/acsami.5b06653>.
- [28] R. Baby, B. Saifullah, M.Z. Hussein, Palm Kernel Shell as an effective adsorbent for the treatment of heavy metal contaminated water, *Sci. Rep.* 9 (2019). <https://doi.org/10.1038/s41598-019-55099-6>.
- [29] X. Huang, M. Pan, The highly efficient adsorption of Pb(II) on graphene oxides: A process combined by batch experiments and modeling techniques, *J. Mol. Liq.* 215 (2016) 410–416.
<https://doi.org/10.1016/j.molliq.2015.12.061>.
- [30] Y. Liu, Y. Xiong, P. Xu, Y. Pang, C. Du, Enhancement of Pb (II) adsorption by boron doped ordered mesoporous carbon: Isotherm and kinetics modeling, *Sci. Total Environ.* 708 (2020) 134918.
<https://doi.org/10.1016/j.scitotenv.2019.134918>.
- [31] K. Yang, Z. Lou, R. Fu, J. Zhou, J. Xu, S.A. Baig, X. Xu, Multiwalled carbon nanotubes incorporated with or without amino groups for aqueous Pb(II) removal: Comparison and mechanism study, *J. Mol. Liq.* 260 (2018) 149–158. <https://doi.org/10.1016/j.molliq.2018.03.082>.
- [32] W. Shen, Q. Da An, Z.Y. Xiao, S.R. Zhai, J.A. Hao, Y. Tong, Alginate modified graphitic carbon nitride composite hydrogels for efficient removal of Pb(II), Ni(II) and Cu(II) from water, *Int. J. Biol. Macromol.* 148 (2020) 1298–1306. <https://doi.org/10.1016/j.ijbiomac.2019.10.105>.
- [33] Y. Long, J. Jiang, J. Hu, X. Hu, Q. Yang, S. Zhou, Removal of Pb(II) from aqueous solution by hydroxyapatite/carbon composite: Preparation and adsorption behavior, *Colloids Surfaces A Physicochem. Eng. Asp.* 577 (2019) 471–479. <https://doi.org/10.1016/j.colsurfa.2019.06.011>.
- [34] G.A. Adebisi, Z.Z. Chowdhury, P.A. Alaba, Equilibrium, kinetic, and thermodynamic studies of lead ion and zinc ion adsorption from aqueous solution onto activated carbon prepared from palm oil mill effluent, *J. Clean.*

- Prod. 148 (2017) 958–968. <https://doi.org/10.1016/j.jclepro.2017.02.047>.
- [35] S.A. Sajjadi, A. Meknati, E.C. Lima, G.L. Dotto, D.I. Mendoza-Castillo, I. Anastopoulos, F. Alakhras, E.I. Unuabonah, P. Singh, A. Hosseini-Bandegharai, A novel route for preparation of chemically activated carbon from pistachio wood for highly efficient Pb(II) sorption, *J. Environ. Manage.* 236 (2019) 34–44. <https://doi.org/10.1016/j.jenvman.2019.01.087>.
- [36] C. Zhang, W. Wang, A. Duan, G. Zeng, D. Huang, C. Lai, X. Tan, M. Cheng, R. Wang, C. Zhou, W. Xiong, Y. Yang, Adsorption behavior of engineered carbons and carbon nanomaterials for metal endocrine disruptors: Experiments and theoretical calculation, *Chemosphere.* 222 (2019) 184–194. <https://doi.org/10.1016/j.chemosphere.2019.01.128>.
- [37] R. Krishnamoorthy, B. Govindan, F. Banat, V. Sagadevan, M. Purushothaman, P.L. Show, Date pits activated carbon for divalent lead ions removal, *J. Biosci. Bioeng.* 128 (2019) 88–97. <https://doi.org/10.1016/j.jbiosc.2018.12.011>.
- [38] H.J. Kim, J.M. Lee, J.H. Choi, D.H. Kim, G.S. Han, H.S. Jung, Synthesis and adsorption properties of gelatin-conjugated hematite (α -Fe₂O₃) nanoparticles for lead removal from wastewater, *J. Hazard. Mater.* 416 (2021) 125696. <https://doi.org/10.1016/j.jhazmat.2021.125696>.
- [39] S. Tabesh, F. Davar, M.R. Loghman-Estarki, Preparation of γ -Al₂O₃ nanoparticles using modified sol-gel method and its use for the adsorption of lead and cadmium ions, *J. Alloys Compd.* 730 (2018) 441–449. <https://doi.org/10.1016/j.jallcom.2017.09.246>.
- [40] Q. Zeng, Y. Huang, L. Huang, L. Hu, W. Sun, H. Zhong, Z. He, High adsorption capacity and super selectivity for Pb(II) by a novel adsorbent: Nano humboldtine/almandine composite prepared from natural almandine, *Chemosphere.* 253 (2020) 126650. <https://doi.org/10.1016/j.chemosphere.2020.126650>.
- [41] L. Zhou, L. Ji, P.C. Ma, Y. Shao, H. Zhang, W. Gao, Y. Li, Development of carbon nanotubes/CoFe₂O₄ magnetic hybrid material for removal of tetrabromobisphenol A and Pb(II), *J. Hazard. Mater.* 265 (2014) 104–114. <https://doi.org/10.1016/j.jhazmat.2013.11.058>.
- [42] Y. Zhang, S. Ni, X. Wang, W. Zhang, L. Lagerquist, M. Qin, S. Willför, C.

- Xu, P. Fatehi, Ultrafast adsorption of heavy metal ions onto functionalized lignin-based hybrid magnetic nanoparticles, *Chem. Eng. J.* 372 (2019) 82–91. <https://doi.org/10.1016/j.cej.2019.04.111>.
- [43] Z. Li, J. Chen, Y. Ge, Removal of lead ion and oil droplet from aqueous solution by lignin-grafted carbon nanotubes, *Chem. Eng. J.* 308 (2017) 809–817. <https://doi.org/10.1016/j.cej.2016.09.126>.
- [44] Ł. Klapiszewski, K. Siwińska-Stefańska, D. Kołodyńska, Preparation and characterization of novel TiO₂/lignin and TiO₂-SiO₂/lignin hybrids and their use as functional biosorbents for Pb(II), *Chem. Eng. J.* 314 (2017) 169–181. <https://doi.org/10.1016/j.cej.2016.12.114>.
- [45] R. Astala, M.J. Stott, First-principles study of hydroxyapatite surfaces and water adsorption, *Phys. Rev. B - Condens. Matter Mater. Phys.* 78 (2008) 1–11. <https://doi.org/10.1103/PhysRevB.78.075427>.
- [46] D.E. Ellis, J. Terra, O. Warschkow, M. Jiang, G.B. González, J.S. Okasinski, M.J. Bedzyk, A.M. Rossi, J.G. Eon, A theoretical and experimental study of lead substitution in calcium hydroxyapatite, *Phys. Chem. Chem. Phys.* 8 (2006) 967–976. <https://doi.org/10.1039/b509254j>.
- [47] M.E. Zilm, L. Chen, V. Sharma, A. Mcdannald, M. Jain, R. Ramprasad, M. Wei, Hydroxyapatite substituted by transition metals: experiment and theory, *Phys. Chem. Chem. Phys.* 18 (2016) 16457. <https://doi.org/10.1039/c6cp00474a>.
- [48] S. V Dorozhkin, Dissolution mechanism of calcium apatites in acids: A review of literature, *World J. Methodol.* 2 (2012) 1. <https://doi.org/10.5662/wjm.v2.i1.1>.
- [49] C. Zhou, X. Wang, X. Song, Y. Wang, D. Fang, S. Ge, R. Zhang, Insights into dynamic adsorption of lead by nano-hydroxyapatite prepared with two-stage ultrasound, *Chemosphere.* 253 (2020) 126661. <https://doi.org/10.1016/j.chemosphere.2020.126661>.
- [50] Y. Zhu, B. Huang, Z. Zhu, H. Liu, Y. Huang, X. Zhao, M. Liang, Characterization, dissolution and solubility of the hydroxypyromorphite-hydroxyapatite solid solution [(Pb_xCa_{1-x})₅(PO₄)₃OH] at 25 °C and pH 2-9, *Geochem. Trans.* 17 (2016) 1–18. <https://doi.org/10.1186/s12932-016-0034-8>.

- [51] S.K. Lower, P.A. Maurice, S.J. Traina, Simultaneous dissolution of hydroxylapatite and precipitation of hydroxypyromorphite: Direct evidence of homogeneous nucleation, *Geochim. Cosmochim. Acta.* 62 (1998) 1773–1780. [https://doi.org/10.1016/S0016-7037\(98\)00098-2](https://doi.org/10.1016/S0016-7037(98)00098-2).
- [52] S. Sugiyama, T. Ichii, M. Fujisawa, K. Kawashiro, T. Tomida, N. Shigemoto, H. Hayashi, Heavy metal immobilization in aqueous solution using calcium phosphate and calcium hydrogen phosphates, *J. Colloid Interface Sci.* 259 (2003) 408–410. [https://doi.org/10.1016/S0021-9797\(02\)00211-4](https://doi.org/10.1016/S0021-9797(02)00211-4).
- [53] R.J. Santucci, J.R. Scully, The pervasive threat of lead (Pb) in drinking water: Unmasking and pursuing scientific factors that govern lead release, *Proc. Natl. Acad. Sci. U. S. A.* 117 (2020) 23211–23218. <https://doi.org/10.1073/pnas.1913749117>.
- [54] J. Li, C. Duan, L. Yuan, Z. Liu, H. Zhu, J. Ren, K. Yan, Recycling Spent Lead-Acid Batteries into Lead Halide for Resource Purification and Multifunctional Perovskite Diodes, *Cite This Environ. Sci. Technol.* 55 (2021) 8317. <https://doi.org/10.1021/acs.est.1c01116>.
- [55] C. Lee, Y. Shin, G.G. Jeon, D. Kang, J. Jung, B. Jeon, J. Park, J. Kim, S.J. Yoon, Cost-efficient, Effect of Low-Quality PbI₂ Purification to Enhance Performances of Perovskite Quantum Dots and Perovskite Solar Cells, *Energies* . 14 (2021). <https://doi.org/10.3390/en14010201>.

국문 초록

조성제어된 생무기물을 이용한 방출된 오염물질 제거

홍 정 석

재료공학부

공과대학

서울대학교

Keyword: Carbonate hydroxyapatite, Whitlockite, wet precipitation, CO₂ absorption, Pb absorption, element modification

Student Number: 2014-22535

환경오염은 21세기 가장 큰 이슈이며, 이를 해결하기 위해 많은 노력이 기울여지고 있다. 화석연료에 의한 대기오염은 지구온난화를 불러일으키고 있다. 지난 40만년간 300ppm 이하를 유지했던 이산화탄소 농도는 이미 400ppm을 초과하였고, 지속적으로 증가하고 있다. 이를 해결하고 화석연료를 대체하여 이산화탄소 발생을 줄이기 위해 재생에너지 개발이 진행되고 있지만, 이미 배출된 공기중의 이산화탄소 또한 회수되어야 한다. 대기오염 뿐만 아니라, 수질오염에서도 문제는 심각하다. 중금속에 의한 수질오염은 오래된 문제이지만 아직 해결되지 못했다. 잘 알려진 중금속인 납은 인체와 생태계에 큰 악영향을 끼친다. 그럼에도 불구하고 납축전지 수요증가와 납을 함유한 석탄의 사용으로 인해 납오염은 심해지고 있다.

환경오염을 해결하기 위해서는 생산부터 후처리까지 전과정을

관리하는 것이 필수이다. 특히 오염 제거제의 생산 및 제거 후처리에서 발생하는 오염은 간과되기 쉽다. 최근 진행된 연구에서도 흡착제 합성과 재생과정에서 높은 에너지 소비와 오염물질 발생이 일어나고 있다. 이산화탄소 흡수의 경우, 대기중의 낮은 이산화탄소 농도가 극복해야 할 한계이다. 일산화 칼슘 (CaO)는 오염물질 제거와 후처리 과정에서 700°C 이상의 높은 온도가 필요하며, 수산화 나트륨 (NaOH)를 이용한 수중침전법 또한 탄산 칼슘 (CaCO₃) 열처리를 포함한 후처리과정에서 900°C 이상의 높은 온도를 필요로 한다.[1,2]

본 연구에서는 전체 정화과정에 대한 전반적인 오염을 제어하였다. 우선, 자연친화적이고 자연친화적으로 합성가능한 생미네랄인 수산화아파타이트 (Hydroxyapatite(HAP))를 선정하였다. 이산화탄소를 제거하기 위해 수산화아파타이트의 인산(Phosphate, PO₄³⁻)를 탄산(CO₃²⁻)으로 조성제어를 하여 문제를 해결하였고, 수중의 납을 제거하기 위해 칼슘 금속 양이온을 마그네슘(Mg) 금속 양이온으로 조성제어를 하였다.

챕터1에서는, 생미네랄을 이용한 대기중 이산화탄소 제거 연구에 대해 논의하였다. 대기중의 이산화탄소 제거를 위해 이산화탄소를 용액에 흡수하여 침전시킬 수 있는 알칼리 금속 중 하나인 칼슘을 이용한 침전법이 이용되었다. 알칼리 금속의 이산화탄소 흡수능력 증대를 위해 알칼리 금속의 수산화물과 발생했을 때 superoxide를 형성하는 과산화수소수(H₂O₂)가 이용되었다. 흡수된 이산화탄소는 탄산 수산화 아파타이트(Carbonate Hydroxyapatite, CHA)를 합성하는데 사용되었고, 이는 탄산칼슘 열처리에 필요한 고온 과정을 회피함으로써 부가적인

환경오염 발생을 억제하였다.

챕터2에서는 HAP를 Mg가 함유된 휘트록카이트(whitlockite, WH)로 조성제어 하였다. 금속 양이온 치환 기작 중 WH에서 주로 일어나는 “용해 & 침전”(Dissolution and precipitation) 기작은 HAP에서 주로 일어나는 이온교환(ionic exchange)보다 훨씬 빠르다. 이를 위해서 HAP 합성과정에서 수산화 마그네슘($Mg(OH)_2$)를 첨가하여 조성제어를 진행하였다. 조성제어를 통해 합성된 휘트록카이트는 성공적으로 용액 내 납이온을 제거하여 고순도, 고결정성을 가진 Hydroxypyromorphite를 형성하였다. 흡수된 납은 간단한 산처리를 통해 요오드화 납(PbI_2)로 처리되어 페로브스카이트 태양전지의 전구체로 활용될 수 있도록 하였다. 단순 분산으로 납을 흡착하고 태양전지 전구체로 활용함으로써 정화과정에서 발생할 수 있는 의도하지 않은 오염물질을 획기적으로 줄이는데 성공하였다.

이 연구에서 대기와 수중으로 방출된 오염물질을 제거하기 위해 조성제어된 생미네랄이 이용되었다. 이산화탄소를 잡기위해 CHA가, 납을 잡기위해 WH가 이용되었다. CHA는 합성과정에서 대기 중 이산화탄소를 흡수하고, WH는 용액 내 단순 분산을 통해 납이온을 제거함으로써 합성과 후처리 과정에서 발생할 수 있는 오염물질 발생을 획기적으로 줄였다. CHA와 WH 합성여부는 XRD 분석법을 통해 확인되었다. CHA의 이산화탄소 제거 및 탄산 치환 여부는 FT-IR 분석을 통해 확인되었다. WH는 HAP에 비해 월등한 납 흡착 성능을 보였으며, ICP 분석을 통해 확인되었다. HAP와 WH의 HPy로의 상변태는 Cs-

TEM분석으로 확인되었다. WH에 흡착된 납은 페로브스카이트 태양전지의 전구체로 활용되었으며, HAP에 흡착된 납이나 상용 전구체로 만들어진 페로브스카이트 태양전지보다 높은 효율을 보였다.

이 연구는 두가지 큰 핵심요소가 있다. 첫째로 방출된 오염물질은 적은 에너지 소모와 오염물질 배출로 잡았다. 이산화탄소는 침전법으로, 납은 단순 교반으로 제거되었다. 둘째로 환경친화적인 생미네랄의 조성을 제어할 통해 환경오염을 제거한 것이다. 조성제어를 통해 인체에 존재하는 친환경적인 물질을 이용함으로써 정화과정 전반에 있어 환경오염을 통제했다는 것이다. 결과적으로 조성제어를 통해 생미네랄의 친환경성을 유지하면서 정화과정 전반에 걸친 경오염을 제거하는데 성공하였다.